Continental Shelf Research 294 (2025) 105530

Contents lists available at ScienceDirect

Continental Shelf Research

journal homepage: www.elsevier.com/locate/csr

Research papers

Analysis of turbulence characteristics in a nearshore area beyond the surf zone of a mesotidal bay

Victor A. Arias-Esquivel, Victor M. Godínez, Markus Gross, Anahí Bermúdez-Romero, Vanesa Magar *

Departamento de Oceanografía Física, CICESE, Carretera Ensenada-Tijuana no. 3918, Zona Playitas, Ensenada C.P. 22860, Baja California, Mexico

ARTICLE INFO

Keywords:
Turbulence
Tidal energy
Reynolds stresses
ADCP

ABSTRACT

Turbulence impacts renewable energy converters' performance due to differences in turbulent kinetic energy (TKE) production and TKE dissipation in estuarine, coastal, and shelf regions. However, the turbulence structure under different environmental forcings is not well understood. This study uses waves, tides, and wind data to analyse the mean flow field and turbulence characteristics in Todos Santos Bay (TSB), a mesotidal bay in the northern Mexican Pacific. The main results are based on a month-long time series obtained with a Sentinel V50, a five-beam Acoustic Doppler Current Profiler (ADCP), installed in a location within the bay where currents are less than 0.55 m s^{-1}. A tidal decomposition analysis of sea level and current data confirmed mixed and predominantly semi-diurnal tides. Waves and wind stresses affect the flow in the layers near the sea surface. We computed the Reynolds stresses, TKE, anisotropy, TKE production and TKE dissipation to characterize the turbulence properties. The zonal vertical Reynolds stress increases from the bottom upwards, while the meridional vertical Reynolds stress decreases from the bottom upwards. The turbulent kinetic energy increases from the bottom upwards. The waves do not significantly affect the Reynolds stresses, the TKE, or the anisotropy ratio when the significant wave height is less than 0.7 m. It is worth highlighting that strong wave conditions have an important effect on the turbulence characteristics of the site, even during spring tides. In addition, turbulent processes change with time following flood and ebb tides in the bay, and the TKE and the zonal vertical Reynolds stress are higher during neap tides than during spring tides. Finally, TKE budget computations showed that TKE dissipation dominates over TKE production, implying the existence of non-local transport to the TKE budget at the site; these turbulence metrics are enhanced during neap tides.

1. Introduction

Turbulence plays a vital role in the production and dissipation of turbulent kinetic energy in estuarine, coastal, and shelf regions. It has important consequences on the conversion of energy from renewable marine energy devices, as turbulence causes an increase in energy power fluctuations, which, in turn, causes a decrease in the efficiency of the tidal energy converter under turbulent conditions (Sentchev et al., 2020). Several authors have analysed turbulence processes in tidal channels, bays, estuaries, and coastal lagoons (Lu and Lueck, 1999b; Rippeth et al., 2002; Nystrom et al., 2007; Burchard et al., 2008; Kirincich and Rosman, 2011; Serio and Mossa, 2015).

Turbulence in the ocean, in general, is affected by environmental forces and stresses caused by surface winds, waves, tides, river discharges, and density gradients (Burchard et al., 2008; McMillan and Hay, 2017; Orton et al., 2010). The complexity of turbulence characterization can be reduced when one forcing factor dominates over the others, at least over one tidal cycle. Analyses under these simpler conditions can provide some understanding of turbulence under more complex situations, for example when non-linear interactions between two forcings such as waves and tides may be of importance.

The first field experiments on turbulence characterization can be traced back to Bowden and Fairbairn (Bowden and Fairbairn, 1952a,b, 1956), who used tidal gauges and bottom-mounted electromagnetic flowmeters to compute velocity fluctuations and Reynolds stresses in tidally-dominated, mostly unidirectional flows. These early studies focused on spectral energy analyses, the relative importance of different spectral frequencies for each velocity component, and the directional dependence of the turbulence integral scales. More recent advances in turbulence measuring techniques based on acoustic instrumentation such as Acoustic Doppler Velocimeters (ADV), or Acoustic Doppler Current Profilers (ADCP) instrumentation combined with the variance method were used to compute flow velocity fluctuations and several

* Corresponding author.
E-mail address: vmagar@cicese.edu.mx (V. Magar).

https://doi.org/10.1016/j.csr.2025.105530
Received 6 August 2023; Received in revised form 17 July 2025; Accepted 17 July 2025
Available online 11 August 2025

turbulence metrics (Lu and Lueck, 1999a,b; Stacey et al., 1999; Rippeth et al., 2002; Guerra and Thomson, 2017; Thiébaut et al., 2020a). Recent technological developments, such as the addition of a vertical beam and an internal inertial motion sensor corrector to ADCP sensors, allow for accurate computations of five of the six Reynolds Stress components (Guerra and Thomson, 2017). All six Reynolds stress components can be computed if two coupled, bottom-fixed and upward-looking ADCPs are used for measuring the flow (Thiébaut et al., 2020c).

Turbulence may be characterized by many metrics, including the Reynolds stresses, the turbulence intensity, the turbulent kinetic energy TKE, the TKE production rate P, and TKE dissipation rate ϵ (which from now on will be simply referred to as P and ϵ), the integral lengthscale L, or the anisotropy coefficient, to name but a few (Sentchev et al., 2020; Thiébaut et al., 2020a,b; Osalusi et al., 2009a,b). In Thiébaut et al. (2020b), for example, the authors installed a system of two coupled ADCPs at the Alderney Race, to compute the vertical profile of the current, the turbulence intensity, all six components of the Reynolds stresses, and the integral lengthscale in all three velocity component directions. This leads to an accurate computation of the TKE, P and ϵ. They found that the ratio ϵ/P was larger than one, that is, the dissipation rate is larger than the production rate at the Alderney Race, a high tidal energy site, throughout the observation. They deduced that non-local transport was important to the TKE budget at the site.

Serio and Mossa (2015) carried out a mean flow and turbulence analysis in a mesotidal bay in the Gulf of Taranto, Italy, using ADCP measurements taken in the surf zone of the Mar Grande Basin. They found that the classical log-law for the vertical velocity profile extended up to 90% of the water column above the seabed, which is unusual. They also computed turbulence statistics using the variance method and determined the temporal evolution of the turbulent mixing throughout the water column. Their findings confirm that both the TKE and the Reynolds stresses generally increase from the seabed to the surface, with jet-shape variations near the surface that can be associated with wave and wind effects. In another study, Orton et al. (2010) evaluated the tidal and atmospheric influences on turbulence in a mesotidal estuary. They confirmed the importance of wind to generate surface shear stress and enhancement on ϵ near the water surface after mixing reduces the stratification of the water column generated by solar heating. They also notice that during spring tides the flow speed increase enhanced TKE, P and ϵ. It is important to note that ebb flow directly enhanced ϵ while the enhancement of P is less evident. In another study, Simpson et al. (2005) evaluated the impact of tidal straining on the cycle of turbulence in a partially stratified micro-tidal estuary. They found that during stratification P is mainly constrained to the mixed layer below the horizontally homogeneous layer during neap tides, but P is enhanced during spring tides due to an increase in the magnitude of flood and ebb tides, normally with stronger dissipation rates in ebb than in flood. All this information leads to the question of how environmental parameters such as wind, waves, currents, and tide flow influence the vertical structure of turbulence in an unstratified water column in the coastal zone without river influence.

Certainly, waves and tides affect turbulence, but it is unclear to what extent the effect of waves and the tidal cycle interact to change the vertical structure of turbulence. Some studies found a partial answer through estimates of dissipation near the top of the water column using three types of platforms: fixed towers, moving ships, and vertical profiling devices such as ADV profilers (Agrawal et al., 1992; Drennan et al., 1996; Soloviev and Lukas, 2003). The first studies evaluated the vertical structure of shear stress and kinetic energy dissipation focused mainly on the ocean surface boundary layer and the effect of wind and breaking waves using a conventional turbulence closure model (Craig and Banner, 1994). Depending on depth, the vertical structure of turbulence dissipation can be interpreted as comprising three distinct layers: (1) a surface wave breaking layer, where TKE is directly injected by breaking waves; (2) an underlying wave-affected layer, where the downward transport of turbulence balances local dissipation; and (3) a deeper layer resembling a classic shear-driven boundary layer, where dissipation is primarily balanced by TKE production from surface wind stress (Terray et al., 1996, 1999). An update in understanding the vertical distribution of dissipation and production in the nearshore water column included the effect of wave orbital velocities and bed roughness using a vertically coupled turbulence (k-ϵ) and mean flow model (Feddersen and Trowbridge, 2005). Additionally, other studies of dissipation confirmed a maximum near the surface, minimum at mid-depth, with a secondary maximum near the bed in shallow waters (Feddersen et al., 2007; Jones and Monismith, 2008). Estuarine turbulence dynamics response to wind-waves effect on the vertical distribution of turbulent kinetic energy, dissipation and turbulent stress (Fisher et al., 2018). Some other studies evaluate TKE dynamics in the ocean surface boundary layer through parametrization models of production, dissipation and transport (Gerbi et al., 2009), while another approach is to apply a model based on barotropic velocity to predict TKE statistics induced by tidal currents (Calvino et al., 2023b,a). In general, these approaches aimed to evaluate TKE dynamics on the ocean surface boundary layer, intermediate water, and the bottom boundary layer, such an approach is possible through the use of ADV installed at different depths. However, the TKE characterization at these boundary layers is constrained when ADCP instruments are used instead of ADV, due to the noise associated with sidelobe interference and the deployment distance above the bottom of the sensor, both limiting the turbulence analysis to intermediate waters, but allow the estimation of time series of turbulence vertical profiles instead of point measurements.

Another question that arises is how these interactions determine or shape TKE distribution, and the TKE balance between turbulent kinetic energy production and dissipation in a mesotidal environment with dynamic wave conditions near a coastal lagoon, and lastly can we detect such changes using an ADCP installed on the surf zone beyond the wave breaking area?. In addition, can this work define the vertical profile of currents and identify a predominant current velocity component near the open end of a coastal environment? Such questions and their answers motivate the research on this work.

Currently, no turbulence characterization studies are available for mesotidal bays such as Todos Santos Bay (TSB), despite the demand for such studies for marine renewable energy applications for environments of different energetic levels (Guerra and Thomson, 2017; McMillan et al., 2016; Thiébaut et al., 2020b). This knowledge gap may be addressed using measurements based on five-beam ADCPs, which allow direct evaluation of vertical velocity fluctuations. Moreover, five components of the Reynolds stress, the TKE, and the anisotropy rate also can be evaluated directly from the ADCP's along-beam velocities (Lu and Lueck, 1999b; Dewey and Stringer, 2017). We aim to use Reynolds stress components, TKE, the TKE production rate P, and the TKE dissipation rate ϵ to identify how waves and tide conditions interact and define the vertical distribution of turbulence in a mainly dissipative environment as a mesotidal bay.

The current work is organized as follows. In Section 2, we introduce the study site, the data collected, the quality control methods, and the methods used to analyse the mean fields. The variance method for the computation of the Reynolds stresses, the turbulent kinetic energy TKE, the production rate P, and the dissipation rate ϵ based on the TKE wavenumber spectrum, are also introduced here. In Section 3 we analyse the mean flow, the wave conditions, and several turbulence metrics. The time depth diagrams of the TKE, Reynolds Stresses, and the TKE production and dissipation rates are discussed in the context of the findings of other authors. We also analyse turbulence characteristics during ebb and flood tides, by identifying four sets of data representing neap and spring tides, and high, medium and small significant wave heights, to explain the mechanisms that can affect Reynolds stresses, TKE, and the TKE budget. The conditions under which turbulence vertical structure is most clearly observed occur during periods of moderate wave height and spring tide, as suggested by our results. These "optimal conditions” refer to times when turbulence is sufficiently strong to exhibit a clear vertical structure influenced by both wave and tidal forcing, but not so energetic as to be dominated by non-linear or highly intermittent processes, such as wave breaking or strong stratification transitions. In this regime, the vertical distribution of turbulence is more stable and quantifiable. Additionally, an error analysis and discussion of Doppler noise, shear stress, Reynolds stress, TKE P, and TKE ϵ is also presented for different wave and tide conditions.

2. Materials and methods

2.1. Study site and monitoring campaign

Todos Santos Bay (TSB) is on the Northeastern Pacific Ocean, on the west coast of the state of Baja California in Mexico, approximately 100 km south of the Mexico-US border. TSB covers an area of 230 km^2 with an average depth of less than 50 m (Alvarez-Sánchez et al., 1988). The site is shown in Fig. 1.

The bay is protected from incoming storms by the Todos Santos Islands, and swell waves can only enter the bay through two oceanic connections. The first connection, on the northern side of the bay, extends from Todos Santos Islands to San Miguel Point for 11 km and has a maximum depth of 50 m. The second connection, on the southern side, extends from Todos Santos Islands to Punta Banda Headland for 5 km and is characterized by a submarine canyon with a depth of up to 400 m.

Surface currents in TSB are dominated by the prevailing winds with observed surface waters moving predominantly to the southeast, into the Bay, following the coastline, in the direction of the wind (Alvarez-Sánchez, 1977). However, currents in the opposite direction were observed as well in the southern region of TSB.

The surface circulation of TSB involves two gyres, one anticyclonic in the north of the Bay and the other cyclonic in the south. A study on drift patterns of Lagrangian tracers confirmed the above-mentioned currents (Alvarez-Sánchez et al., 1988). This feature is supported by similar circulation patterns deduced by the texture of near-shore sediments (Pérez-Higuera and Chee-Barragán, 1984). Other patterns, such as a southward circulation in the north of the Bay, and a northward circulation in the south of the Bay, in front of the Estero de Punta Banda sandbar beaches, have also been observed. Due to the lack of rain in this semi-arid region, no river discharge is associated with the Estero de Punta Banda coastal lagoon.

The TSB is a mesotidal bay (tidal range between 2 and 4 m), based on tidal gauge data from Ensenada’s harbour. Wave parameters have been measured with an AWAC over 3 years (2014–2016), showing a predominance of intense waves during the winter months (Ruiz de Alegria-Arzaburu and Vidal, 2017). The significant wave height, H_s was typically greater than 1.5 m during the winter; the peak wave period, T_p, commonly exceeded 20 s; and the mean incoming peak wave direction, D_p, was of 275 ° — i.e., from the West–North–West, or WNW. A hydrodynamic model describing the general circulation of the TSB showed the presence of two gyres in TSB during the summer, an anticyclonic gyre on the northern part and a cyclonic gyre on the southern part (Mateos et al., 2009), but this model was not validated against in-situ measurements.

A bottom-fixed Sentinel V50 ADCP was installed at the southern side of the TSB, along a transect perpendicular to the mouth of the Estero de Punta Banda, with the transducer head about 0.58 m above the seabed, at the 31.7798 °N, 116.6376 °W geographical point and a depth of 12.6 m, between March 26 and April 24, 2019. Such location was chosen to study the interaction of environmental parameters, such as wind, waves, currents, and the vertical structure of turbulence. The instrument has four JANUS beams slanted at 25 ° from the vertical and a fifth vertical beam. The ADCP was deployed in the surf zone, beyond the wave breaking area of the beach, and it operated in standard dual profiling and wave burst sampling mode, with cells of 0.6 m. Flow velocity acquisition was at 10 min intervals with a sampling frequency of 1 Hz using an average of 180 measurements acquired for three minutes. The wave burst sampling mode, acquired 2099 samples at a frequency of 2 Hz, for 17.49 min every hour. After removing the data associated with instrument installation and retrieval periods, the sampling period was selected from March 26, 19:00 UTC to April 24, 16:20 UTC. The ADCP deployment characteristics and sampling configuration are shown in Table 1.

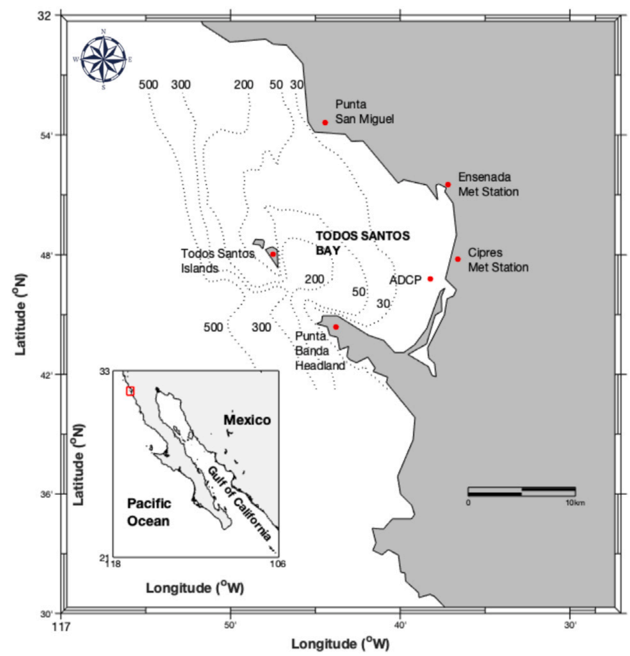

Fig. 1. Study site and monitoring campaign.

Table 1
Summary of ADCP deployment and sampling parameters for waves and currents at Todos Santos Bay, Baja California, Mexico from March 26 to April 24 2019.

ADCP Setup	
Instrument	TRDI Sentinel V50
Latitude (°)	31.7798
Longitude (°)	−116.6376
Water Depth (m)	12.6
Deployment duration (days)	29
Waves	
Sampling frequency (Hz)	2
Burst average (min)	17.49
Currents	
Sampling frequency (Hz)	1
Burst average (min)	10
Bin size △ z (m)	0.6
Number of cells used	12
Distance to the first cell (m)	1.89
Pitch (°)	2.41 ± 0.54
Roll (°)	2.99 ± 1.92

We applied the variance method to compute the turbulence statistics, this is explained in detail in the next subsection.

2.2. ADCP data processing

2.2.1. Wave and sidelobe interference

Waves and currents were processed using Wavesmon and Velocity TRDI ADCP Sentinel V software, respectively. The surface track method was applied to calculate wave spectra and wave statistics. White noise and wave bias were removed during data processing. Data preprocessing included the removal of sidelobe interference and sound reflection due to the interaction of the signal with the waves on the sea surface. Five cells (3 m) below the surface were eliminated, thus reducing the number of total cells to 12, from 2.47 m to 9.07 m above the seabed.

2.2.2. Turbulence analysis

Along-beam velocity components were measured to determine velocity fluctuations and compute the Reynolds stress components, the TKE, P, and ϵ. We applied the variance technique, which assumes that the turbulence is horizontally homogeneous within the sampling volume and that the turbulence statistics are steady over the averaging interval (Nystrom et al., 2007; Kirincich and Rosman, 2011). The first assumption means that while the current flow is not homogeneous, the second-order moments of fluctuating velocities are horizontally homogeneous (Stacey et al., 1999). The variance technique is adequate to directly compute the turbulence characteristics and reduce uncertainty on the Reynolds stress components.

The along-beam velocities components b_i, for a five-beam Janus ADCP, are defined as:

$$b_1 = -u_1 \sin\theta - w_1 \cos\theta \quad (1)$$

$$b_2 = u_2 \sin\theta - w_2 \cos\theta \quad (2)$$

$$b_3 = -v_3 \sin\theta - w_3 \cos\theta \quad (3)$$

$$b_4 = v_4 \sin\theta - w_4 \cos\theta \quad (4)$$

$$b_5 = -w_5 \quad (5)$$

where $\theta = 25°$ is the angle between the acoustic beam centreline and the vertical, and u_i, v_i and w_i are horizontal and vertical velocity components for beam i. All velocities can be split into a mean and a fluctuating part, this is called a Reynolds decomposition. For a five-beam ADCP with non-zero tilt, the Reynolds stress components $\overline{-u'w'}$ and $\overline{-v'w'}$ can be expressed as eqn. (137) and (138) in Dewey and Stringer (2017):

$$\overline{-u'w'} = \frac{\overline{b_2'^2} - \overline{b_1'^2}}{2\sin(2\theta)} + \frac{\phi_3}{\sin^2\theta}\left[\frac{1}{2}\left(\overline{b_2'^2} + \overline{b_1'^2}\right) - \overline{b_5'^2}\right] - \phi_2\overline{u'v'} \quad (6)$$

and

$$\overline{-v'w'} = \frac{\overline{b_4'^2} - \overline{b_3'^2}}{2\sin(2\theta)} - \frac{\phi_2}{\sin^2\theta}\left[\frac{1}{2}\left(\overline{b_4'^2} + \overline{b_3'^2}\right) - \overline{b_5'^2}\right] + \phi_3\overline{u'v'} \quad (7)$$

where ϕ_2 is the pitch and ϕ_3 is the roll. The TKE and the anisotropy ratio α are estimated as

$$TKE = \frac{1}{4\sin^2\theta}\left[\left(\overline{b_1'^2} + \overline{b_2'^2} + \overline{b_3'^2} + \overline{b_4'^2}\right)\right] + \left[-2\left(2\cos^2\theta - \sin^2\theta\right)\overline{b_5'^2} - (\cot\theta - 1)\phi_3\left(\overline{b_2'^2} - \overline{b_1'^2}\right)\right] \quad (8)$$

and

$$\alpha = \frac{2\sin^2\theta\,\overline{b_5'^2} + \cot\theta\,\phi_3\left(\overline{b_2'^2} - \overline{b_1'^2}\right) - \cot\theta\,\phi_2\left(\overline{b_4'^2} - \overline{b_3'^2}\right)}{\overline{b_1'^2} + \overline{b_2'^2} + \overline{b_3'^2} + \overline{b_4'^2} + 4\cos^2\theta\,\overline{b_5'^2} + F(\phi)} \quad (9)$$

respectively, where

$$F(\phi) = \cot\theta\,\phi_2\left(\overline{b_4'^2} - \overline{b_3'^2}\right) + [1 - 2\csc(2\theta)]\,\phi_3\left(\overline{b_2'^2} + \overline{b_1'^2}\right). \quad (10)$$

Neither TKE nor α depend on the unknown stress component $\overline{u'v'}$, hence they can be determined directly, with a correction of up to 20% to remove pitch and roll effects. Beam velocities fluctuations, F(ϕ), and the means of pitch (ϕ_2) and roll (ϕ_3), and TKE wavenumber spectra were calculated with a 9 min average from hourly burst data as further mentioned. Turbulence anisotropy, α, is a rate between vertical and horizontal fluctuation properties of the mean flow. An isotropic turbulent flow satisfies the condition $\alpha = 0.5$. For anisotropic flows, the fluctuating flow properties have a directional preference and the mean velocity flow has a gradient associated with TKE P and ϵ. If $\alpha > 0.5$ then vertical flow structures dominate, if $\alpha < 0.5$ then horizontal flow structures dominate. In an isotropic turbulent flow, full 3D turbulence develops, and the fluctuating flow features have no directional preference; $\overline{u'}$, $\overline{v'}$, and $\overline{w'}$ fluctuations are in balance in the mean turbulent flow with directional independence of turbulence statistics. Anisotropy of the normal stresses is important due to its association with energy transfer from the mean flow through turbulent kinetic energy production and dissipation in an energy transfer cascade from inertial to viscous forces (Vallis, 2017). Common assumed values for turbulence anisotropy oscillate from 0 to 0.50 (Howarth and Souza, 2005; Lu and Lueck, 1999b; Stacey et al., 1999; Milne et al., 2013; Osalusi et al., 2009b).

We used wave burst mode data to get turbulence parameters using a 9 min average selected after testing the differences in the vertical structure of turbulence parameters with 3, 6, 9, 12, 15, and 17.5 min averages. We found that the 9 min average produced vertical profiles that were less noisy and captured the trend well. The computations were performed with open-source codes in Python, Matlab, and spreadsheets to manipulate tabulated binary data. The USGS provided some of the codes (Martini, 2020), while the codes for the turbulence metric computations from raw velocities along the beams were developed in-house using the equations by Dewey and Stringer (Dewey and Stringer, 2017).

Some additional data quality control preprocessing steps were implemented to improve the turbulence analysis. These consisted of removing data falling outside the $\pm 2\sigma$ interval around the mean, where σ is the standard deviation. Then, an interpolation was performed to account for the removed data (typically < 1%); this minimizes the effects of potential bias on the computation of turbulence parameters. Doppler noise and wave bias were also subtracted during data processing and the error associated with calculations of the variance method, TKE production, and TKE dissipation were also considered.

The computations of Reynolds stress and velocity shear components can be combined to determine P :

$$P = -\left(\overline{u'w'}\frac{\partial\overline{u}}{\partial z} + \overline{v'w'}\frac{\partial\overline{v}}{\partial z} + \overline{w'^2}\frac{\partial\overline{w}}{\partial z}\right) \quad (11)$$

where $\overline{u}$, $\overline{v}$ and $\overline{w}$ are the mean velocity components. P indicates the amount of energy that is transferred from the mean flow to the TKE.

The structure-function method, SFM, Wiles et al. (2006) allows the evaluation of P and ϵ. However, results show that the inertial dissipation method, or IDM, gives more reliable values of ϵ than those obtained with the SFM method (Guerra and Thomson, 2017; Thiébaut et al., 2020b). So here we used IDM to evaluate ϵ (Thiébaut et al., 2020b; Guerra and Thomson, 2017; McMillan et al., 2016; Stapleton and Huntley, 1995; Lumley and Terray, 1983). The IDM is derived from Kolmogorov's turbulence hypotheses (Kolmogorov, 1991; Pope and Pope, 2000), and is based on the assumption that if the wavenumbers at which the turbulent energy is produced and dissipated are well separated (the region of separation is known as the inertial subrange), the flux of energy from low to high wavenumber is equal to the dissipation rate, as there are no sinks or sources of energy within the inertial subrange of wavenumbers (Lorke and Wüest, 2005).

TKE wavenumber spectra can be defined as

$$\phi_i(k) = \alpha_i \epsilon^{\frac{2}{3}} k^{-\frac{5}{3}}. \quad (12)$$

Assuming stationarity (based on Taylor's frozen turbulence hypothesis), the inertial subrange of the wavenumber k spectra relates to the frequency f spectra, and Eq. (12) becomes

$$\phi_i(f) = \alpha_i \epsilon^{\frac{2}{3}} \left(\frac{2\pi}{\overline{w}}\right)^{-\frac{5}{3}} f^{-\frac{5}{3}}, \quad (13)$$

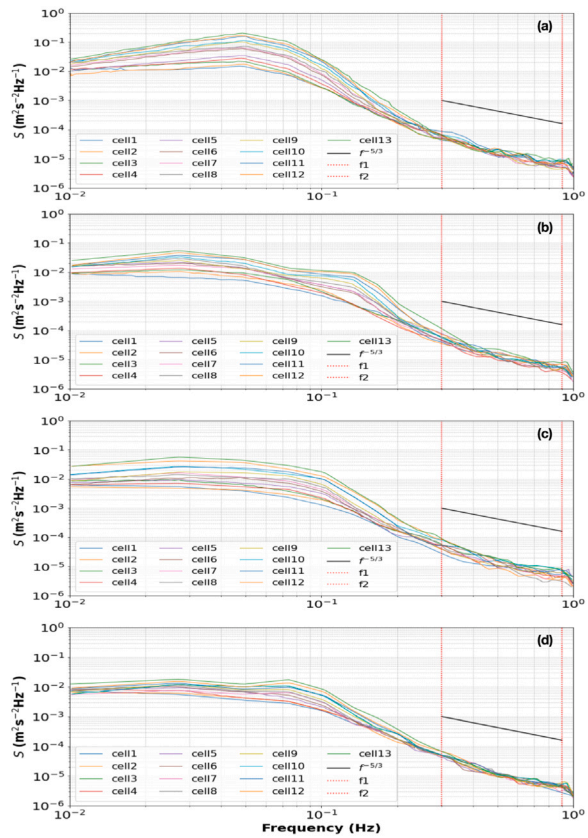

Fig. 2. TKE frequency spectra at different depths: (a) Set 1, (b) Set 2, (c) Set 3, and (d) Set 4 with different waves and tide conditions.

where $\overline{w}$ is the mean vertical velocity. $\phi_i(f)$ is calculated from the measured time series of w, and thus ϵ is estimated by spectral fitting (Lorke and Wüest, 2005; Dewey and Crawford, 1988; Gross and Nowell, 1985). The TKE spectra were estimated using Welch's overlapped segment averaging method. Spectral estimates were calculated for every 9-min burst using twenty-one 50-s sub-windows with 50% overlap which results in an ensemble spectral density estimate with ~41 degrees of freedom (Durgesh et al., 2014). TKE spectra examples are shown for four different wave and tide conditions, as explained below (see Fig. 2).

2.2.3. *Error analysis*

The uncertainties associated with velocity, TKE, shear stress, Reynolds stress, TKE P, and TKE ϵ calculations were estimated following Williams and Simpson equations (2004) (Williams and Simpson, 2004). Doppler noise was approximated as Gaussian white noise with variance σ^2_{NI} estimated from the along beam velocities. The total variance σ^2_N is given by

$$\sigma^2_N = \frac{U}{2\pi}\sum_{I=1}^{4}\sigma^2_{NI} \tag{14}$$

where U is the mean flow speed.

The uncertainties of TKE determinations σ^2_{TKE} are given by

$$\sigma^2_{TKE} = (\sigma^2_N)^2 \tag{15}$$

Shear stress uncertainties are given by

$$\sigma^2_S = \frac{\sigma^2_N}{M\Delta_z^2 sin^2\theta} \tag{16}$$

where σ^2_N is the Doppler noise, M is the number of samples in the burst average, and θ is the beam inclination angle. The uncertainties of the calculation of the Reynolds stress σ^2_R were calculated as

$$\sigma^2_R = \frac{\sigma^4_N}{M\,sin^2 2\theta} \tag{17}$$

TKE P uncertainties σ^2_P were calculated considering the Reynolds stress and the gradient as in

$$\sigma^2_{P_{i,j}} = \overline{v'w'}^2\sigma^2_S + \frac{\partial\overline{u_i}}{\partial x_j}\sigma^2_R + \sigma^2_S\sigma^2_R \tag{18}$$

The total uncertainty σ_P is calculated based on

$$\sigma_P = \sqrt{\sigma^2_{P_{u,w}} + \sigma^2_{P_{v,w}} + \sigma^2_{P_{w,w}}} \tag{19}$$

TKE ϵ uncertainties σ^2_ϵ were calculated as

$$\sigma^2_\epsilon = \frac{2\pi}{\overline{u}}\left(\frac{1}{\alpha}\right)^{\frac{3}{2}}\frac{3}{2}\overline{S_{wcomp}}^{\frac{1}{2}}\sigma_{S_{wcomp}} \tag{20}$$

The sampling period of this study extended for 28.92 days (~694 h), corresponding to yeardays 85 to 114 of the year 2019. Mean flow and turbulence flow characteristics were evaluated for the full series. Four periods of 36 h under contrasting wave and tide conditions were subject to study. The periods were numbered from Set 1 to Set 4 (see Fig. 7). Set 1 corresponds to neap tides (NT) and strong wave conditions, Set 2 to neap tides with medium wave conditions, Set 3 to spring tides (ST) with medium wave conditions, and Set 4 to spring tides with weak wave conditions. Our discussion will mainly focus on Set 4, i.e., the case of weak waves and spring tides, corresponding to the best conditions to evaluate turbulence production and dissipation rates. Note that a sampling period of 28.92 days is sufficient to characterize the dominant diurnal and semi-diurnal components of the tide and, therefore, to separate the tides from the residual currents. However, our tidal analysis approach is limited by the measurement period, and our analysis does not include conditions such as King tides or extreme winter wind-wave forcing. The residual currents and their turbulent fluctuations are the main focus of this paper.

3. Results and discussion

3.1. *Mean flow characteristics*

3.1.1. *Waves*

The hourly wave time series present fluctuations around the mean for the significant wave height H_s, the peak period T_p, and the peak direction D_p, as shown in Fig. 3. The average (range) of H_s, T_p, and D_p were 0.87 m (0.37–2.24 m), 11.1 s (3.3–18.3 s), and 269 ° (239–311 °), respectively. It is important to notice that wave and wind directions are defined based on the meteorological convention, the direction from which they are arriving; while the current directions are defined based on the oceanographic convention, the direction towards which currents flow.

In Figs. 3 and 4 the wind effect on the waves can be observed using wind data from the Ensenada Harbour meteorological station. This station is located in the inner section of the bay inside the harbour, and although some topographic effect by the surrounding hills may be expected, we can neglect this effect because the ADCP location is less than 6 km away from the meteorological station and both sites will be subject to the same wind field forcing (Flores-Vidal et al., 2015). For example, data from El Cipres station are more representative of the local wind at the ADCP location. However, the El Cipres data set has gaps and is only available as a reference. The windrose diagram of Fig. 4a shows the most intense winds have speeds between 10.8 and 14.4 m s^{-1} and blow from the West, followed by winds with speeds of up to 7.2 m s^{-1} blowing from the WSW quadrant (225–270 °).

The waverose diagrams represent the observed H_s and D_p distribution (see Fig. 4b-d). Wave data are divided into all waves, swell waves

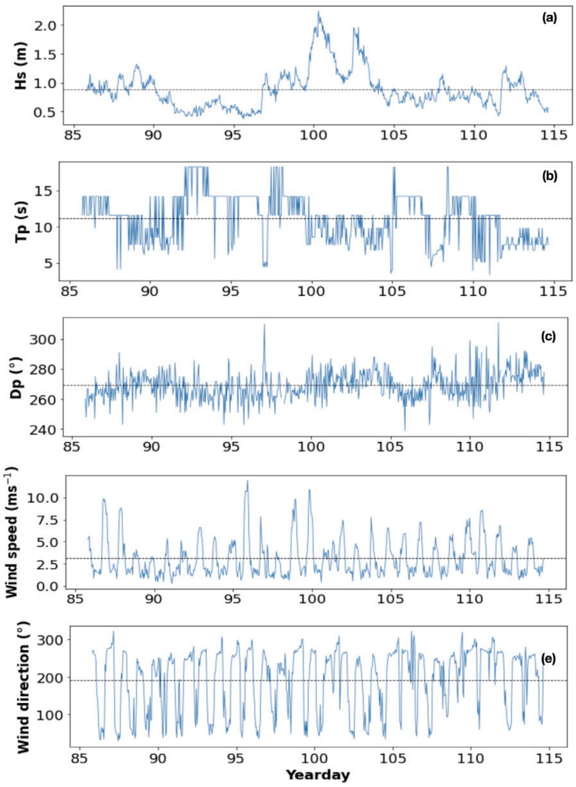

Fig. 3. Wave parameters time series: (a) H_s [m], (b) T_p [s], (c) D_p [° from North] and wind parameters time series: (d) wind speed [m s^{-1}], and (e) wind direction [° from North].

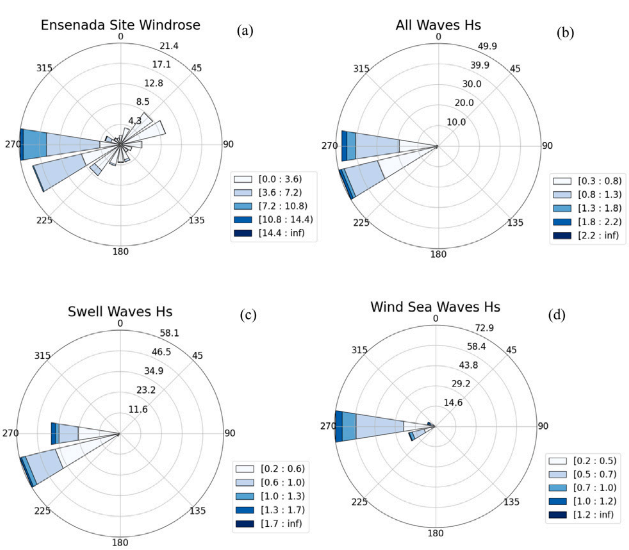

Fig. 4. Windrose of observed wind magnitude and direction at (a) Ensenada site and waverose of a 17.49-min time-averaged, significant wave height, and peak wave direction for (b) All waves (c) Swell waves $T_p > 8$ s, and (d) Wind Sea waves $T_p < 8$ s. All wind and wave direction occurrences are shown in percentage.

($T_p > 8$s), and wind waves ($T_p < 8$s). Such cutoff of 8s corresponds to a wave frequency of 0.125 Hz commonly used on wave characterization (Reeve et al., 2018). However, it is important to note that wave processing parameters to separate wind waves from swell waves were performed using wave energy spectra. In all the waverose diagrams, the two main wave directions agreed with the wind directions previously found, but with differences in wave distribution. Most waves arrive from the West and the WSW direction quadrants (47% and 50%, respectively) with H_s being up to 2.2 m (see Fig. 4b). 58% of the incoming swell waves arrive from the WSW, compared to 39% from the West; for swell waves, H_s is up to 1.7 m (see Fig. 4c). In contrast, 73% of wind waves come from the West, and only 18% come from the WSW quadrant (225–270°); the H_s for wind waves is of up to 1.2 m (see Fig. 4d). In addition, a correlation analysis performed to compare waves to wind parameters shows that H_s and T_p are linked to wind speed with $r^2 = 0.55$ and 0.65, respectively with a 95% confidence interval for the 694 h time series. In contrast to what we observed when comparing waverose and windrose diagrams wave direction is unrelated to wind speed and wind direction. In addition, wind speed to wind direction correlation is low ($r^2 = 0.33$). These differences could be explained by the fact that the energy transfer by wind stress to wave formation and displacement in the area responds to a combination of factors such as wave diffraction and refraction influenced by bottom bathymetry and that wave formation response to wind forcing is not always linear or instantaneous plus the fact that swell waves are not generated by local wind (Durazo et al., 2024).

However, the predominance of westward directed wind waves is corroborated by measurements of local winds at the Ensenada Harbour met station. Based on the study by Hasselmann and Olbers (Hasselmann and Olbers, 1973), H_s and T_p were calculated from the wind speed using the JONSWAP method, corroborating the existence of wind waves with a predicted H_s that ranged between 1.5 and 3 m. Such wind waves can enhance the current velocities near the sea surface. We identified yeardays 88, 89, 97, 100, 101, 103, 105, 111, and 112 as days when the effect of wind waves and wind on current velocities near the surface may be strongest (see Fig. 3a and 3d). This combined effect is commonly observed as an increase in the velocity just below the water surface. During the preprocessing of our data, we eliminated the data in the top three metres below the surface and corrected the data to eliminate sidelobe interference and surface reflection, to reduce wind wave effects on tidal currents. This step helps to reduce the noise associated with waves near the surface eliminating the bias introduced by wind waves on turbulence parameters calculations (Osalusi et al., 2009a; Stacey et al., 1999).

Our current speed time-depth diagrams appear to indicate we have a reduced influence of waves in the form of lobular intensification close to the surface. It is common to find current speeds that increase from 0.50 m s^{-1} to more than 1.5 m s^{-1} in the top 5 m of the ocean, at sites with a water depth of 40 m (Abdessalem et al., 2013). The lack of evidence of wave effects on the current speed during strong wave events appears to indicate that our data-cleaning protocol to remove wave bias was adequate.

3.1.2. *Currents*

Fig. 5 shows current speed and direction time-depth diagrams, together with water elevation fluctuations around the mean sea level, over the measuring period. High mean current speeds are associated with spring tides and low mean current speeds with neap tides (see Fig. 5a). The tidal currents direction displays a strong North–South orientation at the deployment site (see Fig. 5b), and mostly with currents in the Northward direction. This is to be expected, as we are located in the southern part of the Bay and relatively close to the shore. Table 2 shows that the average current speed changes very little in the vertical direction. The current direction also changes very little in the vertical, from 328° near the seabed to 298° near the surface. The current speed maximum may take values of 0.39 m s^{-1} at the seabed, and values of 0.55 m s^{-1} near the sea surface (see Fig. 5a).

Fig. 6a of u, v, and w depth-averaged velocity components shows that the vertical velocity is smaller than the zonal and meridional components of the current velocity, as one would expect in shallow coastal zones. We found velocity component means of 0.007, 0.005, and 0.002 m s^{-1}, respectively. The velocity components range from −0.34 to 0.24 m s^{-1} for u, −0.37 to 0.24 m s^{-1} for v, and −0.023 to 0.086

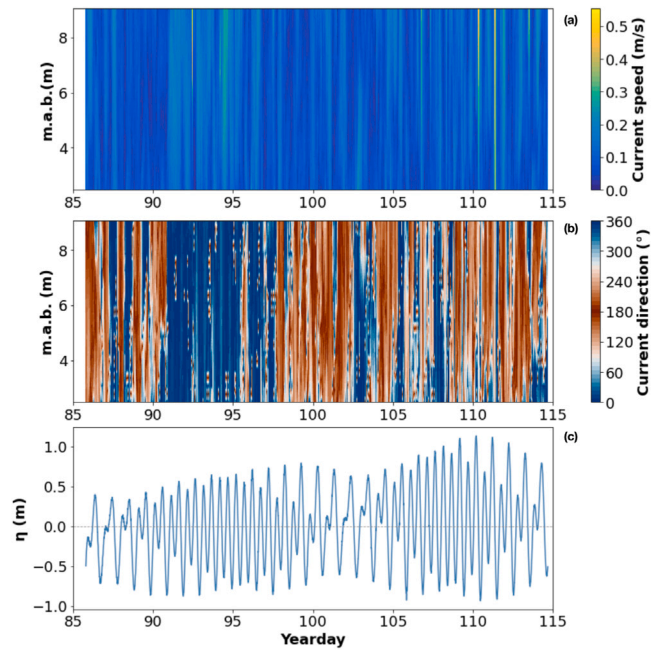

Fig. 5. Hourly time-depth diagrams of currents and sea level over the period of observation: (a) Current speed, (b) Current direction, and (c) Free surface elevation, η, around mean sea level (MSL).

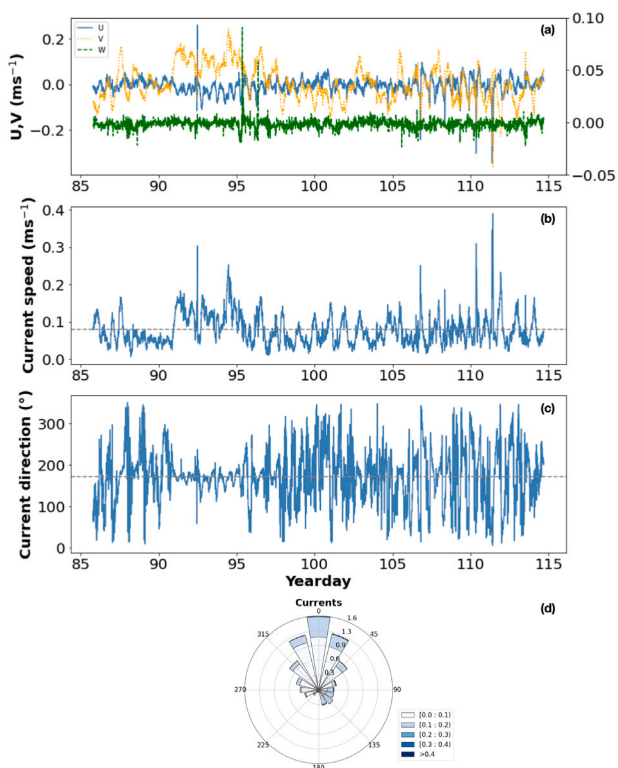

Fig. 6. Depth-averaged time series of current parameters over the observation period: (a) u, v, and w, with mean of −0.71, 0.50, and −0.17 cm s^{-1}, respectively (b) Current speed with mean of 7.76 cm s^{-1}, (c) Current direction with mean of 188.22°, and (d) Currentrose of flow speed and water direction.

m s^{-1} for w. Fig. 6b and 6c show the depth-averaged current speed and direction fluctuations around the mean, which have mean values of 7.76 cm s^{-1}, and 188.22°, respectively, and ranges of 0.007–0.39 m s^{-1} and 5.28–355.64°, respectively. Note that velocity components, and the

Table 2
Mean current speed and direction per cell (and cell's central height) over the observation period.

Cell	Speed (m s^{-1})	Direction (°)	mab (m)
cell 12	0.089 ± 0.055	298.70 ± 172.48	9.07
cell 11	0.087 ± 0.054	290.54 ± 153.97	8.47
cell 10	0.085 ± 0.053	286.68 ± 141.92	7.87
cell 09	0.083 ± 0.052	284.86 ± 136.57	7.27
cell 08	0.081 ± 0.050	282.70 ± 137.47	6.67
cell 07	0.079 ± 0.049	285.50 ± 134.56	6.07
cell 06	0.077 ± 0.048	288.77 ± 134.14	5.47
cell 05	0.075 ± 0.046	295.28 ± 136.46	4.87
cell 04	0.073 ± 0.044	304.62 ± 144.48	4.27
cell 03	0.070 ± 0.042	315.60 ± 131.87	3.67
cell 02	0.068 ± 0.040	323.22 ± 115.30	3.07
cell 01	0.065 ± 0.038	328.04 ± 103.55	2.47

speed and direction, are calculated for each cell in the profile. Depth averaged velocity components are obtained for each profile and depth averaged current speed and direction are obtained for each profile considering each velocity component. Once the profiles for speed and direction are calculated, then the depth-averaged values are obtained per profile.

The current speed and direction distribution are presented in a current rose diagram in Fig. 5d. This diagram shows clearly the dominance of the N, NEN, and NWN currents (in order of importance). When considered together, 46% of the currents move to the N-NEN-NWN direction, and thus we found a longshore current moving northward in the southern part of the TSB, in agreement with Alvarez-Sánchez et al. (1988), based on experiments with Lagrangian drifters. Moreover, Alvarez-Sánchez et al. (1988) observed that near the mouth of the Estero de Punta Banda, there is a convergence zone of northward and southward currents and that currents between March and August are generally strong, with speeds of around 15 cm s^{-1}. Our work shows that the currents are weak, with a mean speed of around 7 cm s^{-1}, but the ADCP deployment was close to the Estero de Punta Banda, and thus being close to the zone of convergence of northward and southward currents may be behind the weak flow speeds we obtain.

Current speed and water elevation (η) time series were subject to harmonic spectral analysis to extract the main tidal harmonic constituents using t_tide (Pawlowicz et al., 2002). The spectral analysis of η identified the diurnal tidal components K1 and O1 with amplitudes of 0.2454 m and 0.2069 m; and the semidiurnal tidal constituents M2 and S2 with amplitudes 0.4822 m and 0.27 m, respectively. The semi-diurnal components are larger than the diurnal ones, confirming the semi-diurnal behaviour of the tides in the TSB. From the spectral analysis of current speeds, we obtained the speeds associated with the tidal components: 1.16 cm s^{-1} for M2, 1.13 cm s^{-1} for S2, 0.66 cm s^{-1} for K1, and 0.74 cm s^{-1} for O1. The tidal form number:

$$F = \frac{K1 + O1}{M2 + S2} \tag{21}$$

is 0.6, and is associated with a mixed, mainly semidiurnal tide, in agreement with the findings of previous studies in the TSB (Defant, 1961; Dronkers, 1964; Flores-Vidal et al., 2015; Lee and Chang, 2019). The constituents M3, MK3, M4, MS4, and 2SM6, were also found relevant at the location of observation in the TSB. Hence, nonlinear interactions between the M2, S2 and K1 tidal constituents also affect the coastal dynamics in this region.

A correlation analysis compares the tide signal from the water level against the tide signal from the current speed series. In the former we used η original and η tide signal series; in the latter, we used the original, residuals, and tide signal series of current speed to identify any link among them. In the case of current speed, a t_tide analysis extracts the tide signal from the original current speed signal series. The residual signal is the remaining from the original signal minus the tide signal. The results showed no significant correlation between tide and currents for the 694 hr time series. Although this may indicate that the observed currents are not tidal, some other processes may be in place, such as bathymetry that hampers the tide analysis. For example, we are probably detecting a longshore current that has also been observed around our sampling location in previous studies (Alvarez-Sánchez et al., 1988; Alvarez-Sánchez, 1977). In addition, the performed harmonic analyses predict only ~28% and ~12% of the original signal variance of u and v velocity components, respectively, meaning that at least ~60% of the variance is lost in the tide analysis. We also use single value decomposition (SVD) analysis on the current parameters to elucidate how much the tides are correlated with the currents and we found that after comparing results from 4 different eigenvalues which together explain ~85% of the variance of currents, no significant correlation could be found between tides and currents. These results may indicate that a more specific analysis should be performed with shorter time intervals based on different wave and tide conditions.

If we compare the current parameters among themselves using the current tide signal and current residuals series we corroborate that current direction and the u velocity component are significantly linked ($r^2 = 0.79$ and $r^2 = 0.36$, respectively). A correlation analysis based on the eigenvalues obtained to compare currents among themselves corroborates that the main correlation is between the current direction and u velocity component with $r^2 = 0.52$.

This correlation found between current speed and the u velocity component was further investigated by using the tide reconstruction function from t_tide (Pawlowicz et al., 2002) to plot the tidal ellipse for the 694−hr tidal current time series and we identify the u velocity component as the major axis of the tidal ellipse which corroborates the link among current direction and u velocity component meaning that a tidal current is present in the NW-SE direction in alignment with the predominant velocity component of the tidal ellipse. However, if a longshore current is present in the area with a predominant northward direction the fact that the current direction and current speed are not related to the v velocity component may indicate that we have a tidal current flowing along the longshore current and we may need to look for specific tide condition to see if we can identify other correlations among current parameters. Such an approach will be undertaken in the following sections.

3.2. Turbulent flow characteristics

Turbulence is generated by shear stress driving instabilities in the mean flow that promote turbulent kinetic energy production. The production rate P is a measure of the energy flux from the mean flow field to the fluctuating flow field. This energy can follow the energy cascade from large to subsequently smaller eddies until molecular diffusion dissipates energy into heat transfer. This energy flux from TKE to heat is where the inertial subrange is located and the dissipation rate ϵ is a measure of it. The TKE budget is relevant for many ocean processes such as stratification and mixing, and for wave and current energy conversion applications. Small-scale turbulence plays an important role in sediment transport and many life processes of planktonic organisms (Sentchev et al., 2020; Sun et al., 2020). Concerning sediment transport, the vertical profile of suspended particulate material concentrations is closely linked to the current's vertical profile (Orton et al., 2010; Mariotti and Fagherazzi, 2011; Nowacki and Ogston, 2013). However, going into more detail about the suspended sediment dynamics in our study site is beyond the scope of this paper.

As previously described, we used the variance technique, based on Dewey and Stringer equations, to estimate turbulence parameters, after a rigorous data quality control to remove outliers and noise associated with Doppler measurements. In Section 3.2.1, the vertical structure of turbulence will be analysed through the general characteristics of the Reynolds stresses components, the turbulent kinetic energy TKE, and the anisotropy ratio α. In Section 3.2.2, a TKE budget, based on the difference between the TKE production rate, P, and dissipation rate, ϵ, will also be presented and discussed. Finally, in Section 3.2.3, we present an analysis of tidal flow, waves and turbulence during flood and ebb tides. Tidal asymmetry plays an important role in tidal current energy production and so does turbulence. Therefore, a characterization of turbulence and the effect of tidal asymmetry on turbulence during different wave and tidal regimes is relevant for offshore renewable energy research.

3.2.1. Reynolds stresses, turbulent kinetic energy, and anisotropy ratio

Fig. 7 shows the depth-averaged and time-depth diagrams during the observation period of the Reynolds stress components $\overline{u'w'}$ and $\overline{v'w'}$, the TKE, and α. The Reynolds stresses and the TKE are larger between yeardays 100 and 103 than in the rest of the observation period; during these yeardays we have neap tides and strong wave conditions. $\overline{u'w'}$, depicted in Fig. 7a–b, increases from the seafloor to the surface. In contrast, $\overline{v'w'}$, depicted in Fig. 7c–d, has an opposite tendency. Such contrasting tendencies in Reynolds stresses are uncommon. The $\overline{u'w'}$ Reynolds stress decrease with depth due to the decay of turbulence and reduced momentum transport by turbulent eddies. As TKE attenuate with depth the $\overline{u'w'}$ Reynolds stress also decrease. The $\overline{v'w'}$ is dominantly influenced by vertical redistribution of meridional momentum and the Ekman spiral, increasing towards the surface due to stronger Coriolis-induced effects and surface turbulence. However, an opposite tendency exists for $\overline{v'w'}$ and a possible explanation is that in this shallow zone the meridional momentum is dominated by the meridional shear stress; here a longshore current dominates near the bottom, with the Ekman spiral possibly being attenuated in this shallow area where currents are less than 0.55 m s^{-1}.

In general, $\overline{u'w'}$, and $\overline{v'w'}$ time series display similar range of values, while $\overline{u'w'}$ and $\overline{v'w'}$ mean values are 2×10^{-3} m^2 s^{-2} and 9.5×10^{-4} m^2 s^{-2}, respectively. Depth-averaged time-series profiles range from −4.1 to 20.4×10^{-3} m^2 s^{-2} for $\overline{u'w'}$ and from −8 to 16.4×10^{-3} m^2 s^{-2} for $\overline{v'w'}$ (see Fig. 7a–d). It is also clear that in the presence of strong waves and neap tides, both shear stresses are enhanced (see Set 1 in Fig. 7a–d). In addition, the average Reynolds stress time-depth diagrams display contrasting behaviour in the water column as mentioned above for $\overline{u'w'}$ and $\overline{v'w'}$ with average ranges from −0.5 to 5.2×10^{-3} m^2 s^{-2} and 1.7 to -0.4×10^{-3} m^2 s^{-2}, respectively.

Fig. 7e–f shows the depth-averaged and the time-depth diagram of TKE over the observation period, while Fig. 7g–h shows the depth-averaged and the time-depth diagram of anisotropy ratio α. As one would expect, the flow is more isotropic ($\alpha = 0.5$) when TKE is small, and more anisotropic ($0.5 < \alpha < 0.5$) when TKE is larger. However, during yeardays 100–104, when TKE is the largest for the yeardays, we see a clear difference in anisotropy over the water column, with large isotropy near the surface and large anisotropy near the bottom. The average flow is mainly anisotropic for the whole time series (see Fig. 7g). Over the period of observation, the TKE mean is 10.1×10^{-3} m^2 s^{-2}, but the average profile varies between 7 and 14.6×10^{-3} m^2 s^{-2} over the water column. TKE depth-averaged range from 0.3 to 63.2×10^{-3} m^2 s^{-2}, as shown on Fig. 7e. As previously mentioned the period of intense waves and neap tides enhance TKE and isotropy associated with Reynolds stress enhancement near the surface as can be seen from Fig. 7e–h. From Fig. 7h, showing the anisotropy ratio time-depth diagram, we observe more anisotropy near the bottom, increasing toward more isotropic values near the surface with isolated anisotropic areas (in red) with a pivot point of 0.5 (isotropy), where above and below 0.5 we have anisotropy with horizontal forcing dominating when $\alpha < 0.5$ and vertical forcing dominating when $\alpha > 0.5$. The anisotropy ratio average is 0.30 with an average mean profile range from 0.19 to 0.46 and an anisotropy time series depth-averaged range from 0.10 to 0.62 (see Fig. 7g).

Our Reynolds stresses and TKE results agree in general with those from a study on a Bay in the Gulf of Taranto, Italy, subject to similar wind, waves, and current conditions (Serio and Mossa, 2015). De Serio and Mossa [7] found Reynolds stresses in the range of 0.1 to 0.75 ×

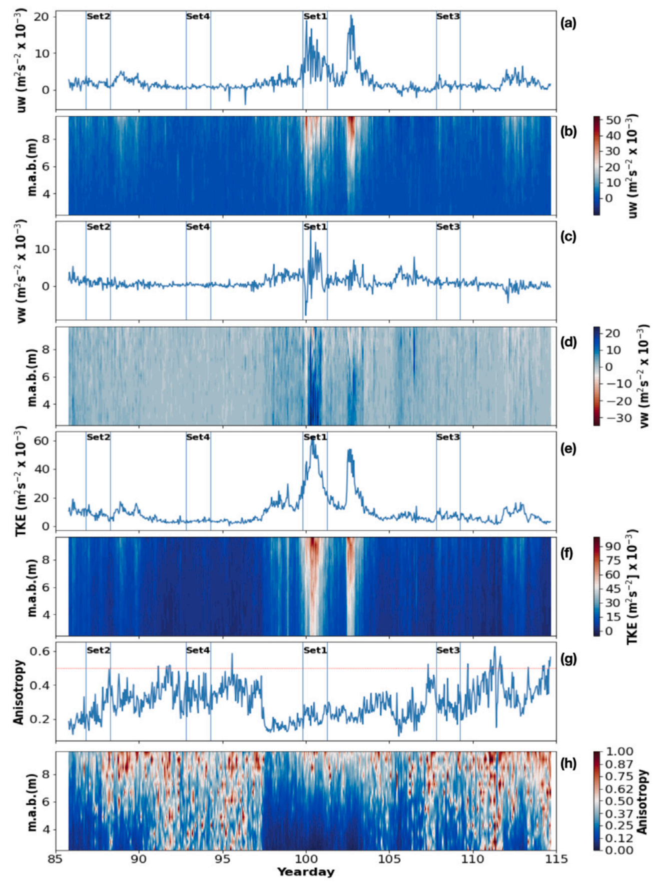

Fig. 7. Depth-averaged time series and time-depth diagrams of hourly turbulence parameters: Reynolds Stress components (a) $\overline{u'w'}$ and (c) $\overline{v'w'}$, (e) TKE, and (g) anisotropy ratio α. Vertical change of hourly turbulence parameters: Reynolds Stress components (b) $\overline{u'w'}$ and (d) $\overline{v'w'}$, (f) TKE, and (h) anisotropy ratio α.

10^{-3} m^2 s^{-2} and TKE in the range of 5 to 10 $\times$ 10^{-3} m^2 s^{-2}, similarly, the mesotidal bay has *u, v, w* velocity components in the range of –0.40 to 0.13 m s^{-1} with an increase in the magnitude of Reynolds stresses, TKE and current speeds from bottom to surface.

Simpson et al. (2005), based on ADCP and CTD measurements in a micro-tidal estuary, found shear Reynolds stresses with values up to 63 $\times$ 10^{-3} m^2 s^{-2}, with tidal currents of 1 m s^{-1} and 0.4 m s^{-1} on flood and ebb tides, respectively. They studied the effect of tidal straining on the cycle of turbulence. They found that stratification during neap tides hinders the development of turbulence and limits the turbulent flow below the stratified section of the estuary. On the contrary, during spring tides with faster tidal currents, the mixing of the whole water column enhances TKE transfer from the mean flow with the shear stress development that enhances production.

Some contrasting Reynolds stresses and TKE range of values are observed for other environment dynamic conditions, such as tidal channels or environments under intense wave influence, where current speeds can reach up to 4 m s^{-1}, or where H_s can be greater than 3 m, respectively. To evaluate turbulence in such environments, it is essential to choose data sections where the time series correspond to waves with H_s < 0.7 m or to apply filtering methods to remove wave frequencies corresponding to gravity waves (McMillan and Hay, 2017; Thiébaut et al., 2020a; Kirincich et al., 2010). For example, Thiébaut et al. (2020b) and De Serio and Mossa (Serio and Mossa, 2015) use sections of 36 h of data where H_s and T_p satisfy the previous requirement, while McMillan and Hay (McMillan and Hay, 2017) and Kirincich et al. (2010) use a co-spectral fitting method to reduce the wave effect on turbulence.

Another exciting aspect to discuss is the value of anisotropy. The assumed value of 0.17 used in previous studies with the variance method was common practice applied while working with four-beam ADCP current data (Stacey et al., 1999; Lu and Lueck, 1999b; Nystrom et al., 2007). In our research, we can measure the variance of *w*, which allows a straightforward determination of anisotropy and total TKE. The uncertainty and bias resulting from the inferences used to determine the TKE by assuming an anisotropy ratio instead of its direct evaluation is the main advantage of using a five-beam ADCP. In our study, values closer to zero or when α < 0.5 represent the onset of anisotropy where horizontal fluctuating velocity components dominate and the average values found for anisotropy range from 0.10 to 0.19. It is worth noting that when the anisotropy ratio is close to 0.5, the turbulence flow is isotropic.

In an attempt to approximate the possible effect of environmental processes such as waves, wind, tides, and currents on the development of the turbulence vertical structure, different parameters of the previous processes were subject to a correlation analysis using the 694 h time series as a first approximation. In general, results indicate that H_s is the only wave parameter linked to $\overline{u'w'}$ and TKE with r^2 = 0.59 and r^2 = 0.82, respectively. Wind speed and wind direction are unrelated to any turbulence parameter. Tide signal from sea level is unrelated to turbulence. All the previous results correspond to the original series of turbulence parameters.

The residual and tide signal from the currents and turbulence parameters yield similar results with H_s as the only wave parameter linked to $\overline{u'w'}$ and TKE with r^2 = 0.28 and r^2 = 0.44, respectively for the residual series and r^2 = 0.37 and r^2 = 0.39, respectively for the tide signal series. It is clear that there is a link between waves (H_s) and turbulence mainly $\overline{u'w'}$ and TKE, but the correlation is weaker in the residual and tide signal series comparisons with respect to the original series comparisons. Currents parameters are all unrelated to the original, residual, and tide signal series of the turbulence parameters although current speed is slightly linked to $\overline{u'w'}$ and TKE with r^2 = 0.31 and r^2 = 0.27, respectively for the tide signal series. These results confirm that turbulence in this mesotidal bay is dominated mainly by the wave interaction indicated by wave H_s on the nearshore area close to Estero de Punta Banda.

A Single Value Decomposition (SVD) analysis was used to correlate the different eigenvalues approximation series of turbulence with waves, wind, tides and currents using up to 4 eigenvalues. The approximation of the first eigenvalue yield correlations between H_s and $\overline{u'w'}$ and TKE with r^2 = 0.58 and r^2 = 0.82, respectively. Such results are quite similar and confirm H_s as the main parameter linked to turbulence. The approximation of the second eigenvalue yield correlations between H_s and $\overline{v'w'}$ and anisotropy with r^2 = 0.15 and r^2 = 0.43, respectively. Anisotropy is linked to wave effects. The remaining eigenvalue approximations (3–4) yield no correlation of any wave, wind, tide, and current parameter with turbulence. It is clear that waves are linked to turbulence at least for the whole 694 h time series evaluation, but even if no correlation appears concerning tide and currents we think that a similar approach using a shorter series of time with different wave and tide conditions may yield further information.

For example, in the time series of turbulence parameters, it is possible to identify time sections where Reynolds stresses, TKE, and anisotropy ratio are associated with different levels of turbulence intensity. Intense turbulence is observed on yeardays 86–90, 97–104, and 112–114, while less turbulence is present on the remaining days. Turbulence is affected by the spring-neap tidal cycle, based on a tidal harmonic analysis of the turbulence.

Wave–current interactions could affect turbulence. This effect is well known and co-spectral filtering could be used to remove the wave influence. However, it is worth analysing contrasting wave conditions, under neap and spring tides. For example, a comparison of yeardays of intense turbulence with wave conditions during those days shows that

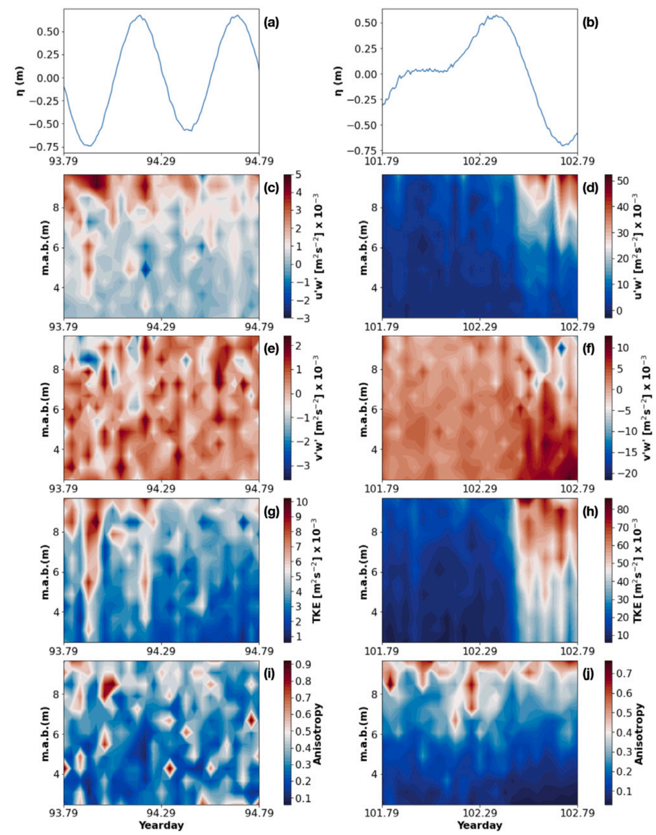

Fig. 8. Free surface elevation, η, around mean sea level (MSL) (a) and (b). Time-depth diagrams of turbulence parameters (c) to (j): Reynolds stresses $\overline{u'w'}$ (c) and (d), $\overline{v'w'}$ (e) and (f), TKE (g) and (h), and anisotropy ratio (i) and (j), under low (yeardays 93–94) and high (yeardays 100–101) TKE conditions.

the intensification of turbulence observed during neap tides is also associated with significant wave heights greater than 1 m. Some researchers choose to identify the section where H_s is small (< 1 m) in their time series, to characterize turbulence parameters under weak wave conditions defining the absence of wave influence with an amplitude spectrum (Serio and Mossa, 2015; Thiébaut et al., 2020a). However, we were interested in the first approach to the turbulence distribution over the entire measurement period to identify the possible effect of waves on turbulence at TSB. Because it is clear that H_s from 1 to 3 m affects surface current velocities (Kirincich et al., 2010; Rosman et al., 2008). We decided to compare two 24-hour periods of contrasting turbulence intensity. The less intense turbulence period refers to yeardays 93–94 with H_s < 0.75 m, and the more intense period refers to yeardays 100–101 with H_s > 1 m. These periods overlap with Set 4 (spring tides and weak waves) and Set 1 (neap tides and strong waves) representing contrasting tide and wave conditions (see Figs. 3 and 5).

The time-depth diagrams of the turbulence parameters over 24 hr periods for different levels of turbulence intensity display notable differences (see Fig. 8). It is possible to identify how turbulence vertical structure changed with time due to flood and ebb tide on the bay. However, the tidal effect is not as evident as on tidal channels, characterized by intense flood and ebb currents where tidal currents modulate time series of Reynolds stresses (Thiébaut et al., 2020b; Rippeth et al., 2003). The lack of correlation among tide, currents, and turbulence previously found confirms this statement. Nevertheless, it is clear that during the 100–101 yeardays, the intensification of turbulence enhances Reynolds stresses, and TKE vertical structure change over time (see Fig. 8). Another notable difference between these two periods of turbulence intensity is that the Reynolds stresses and the TKE values are one order of magnitude larger under the high TKE conditions than on the low TKE conditions.

Reynolds stresses $\overline{u'w'}$ and $\overline{v'w'}$ are much larger on 100–101 yeardays than on 93–94 yeardays (see Fig. 7a-d, Set 1, Set 4) with depth-averaged mean profiles not only one order of magnitude larger on the former yeardays interval (6.8 and 1.5 × 10^{-3} m^2 s^{-2} (Set 1) and 7.7 and 2.0 × 10^{-4} m^2 s^{-2} (Set 4) for $\overline{u'w'}$ and $\overline{v'w'}$, respectively), but also the contrasting behaviour between $\overline{u'w'}$ and $\overline{v'w'}$ in the water column is preserved, but with clear differences in magnitude (−1.6 to 51.2 and −20.8 to 12.2 × 10^{-3} m^2 s^{-2} (Set 1) and −2.9 to 4.8 and −3.44 to 2.25 × 10^{-3} m^2 s^{-2} (Set 4) for $\overline{u'w'}$ and $\overline{v'w'}$, respectively) for both yeardays intervals. Time series mean profiles range from 0.9 to 20.4 × 10^{-3} m^2 s^{-2} for $\overline{u'w'}$ and from −1.2 to 4.3 × 10^{-3} m^2 s^{-2} for $\overline{v'w'}$ on Set 1, while on Set 4 it range from −0.5 to 14.8 × 10^{-4} m^2 s^{-2} for $\overline{u'w'}$ and from −5.3 to 9.9 × 10^{-4} m^2 s^{-2} for $\overline{v'w'}$.

Total TKE average mean profiles are larger for 100–101 yeardays (24.9 × 10^{-3} m^2 s^{-2}) than for 93–94 yeardays (3.8 × 10^{-3} m^2 s^{-2}) with low intensities near the bottom, increasing toward the surface. On the water column Set 1 range from 17.1 to 33.7 × 10^{-3} m^2 s^{-2} while on Set 4 range from 2.3 to 5.8 × 10^{-3} m^2 s^{-2}. The TKE mean profile range from 11.6 to 54.1 × 10^{-3} m^2 s^{-2} (Set 1) and 2.5 to 6.6 × 10^{-3} m^2 s^{-2} (Set 4).

The anisotropy average on 100–101 yeardays is 0.22 and the anisotropy mean profiles range from 0.17 to 0.28. On yeardays 93–94 the anisotropy average is 0.33, with anisotropy mean profiles range from 0.21 to 0.47. Anisotropy is stronger in the Set 1 than in the Set 4 time series.

These differences in turbulence intensity in the average mean profiles observed in the previous comparison confirm the need to select the method to estimate Reynolds stresses with care. The variance method is known to be robust in relatively calm conditions, but is susceptible to the effect of waves on the estimation of Reynolds stresses when H_s is between 1 to 3 m, and our results confirm a bias in Reynolds stresses and TKE estimation on the 100–101 yeardays when H_s is up to 2.2 m.

A spectral analysis of each of the 24–hr intervals results in no evidence of the presence of gravity waves in the amplitude spectra of Set 4 while it does in Set 1. These results confirm that the increase in turbulence is due to wave interaction on Set 1. In addition, a correlation analysis to compare waves, wind, tide, and currents with turbulence for each set yielded a significant correlation of H_s with TKE only for Set 1 (r^2 = 0.76) while on Set 4 no significant correlation was found with any turbulence parameters. However, we found that several current parameters are linked between them. On Set 1 current speed is related to the v velocity component (r^2 = 0.90) while the current direction links to u and v velocity components (r^2 = 0.55 and r^2 = 0.45, respectively). Similarly, Set 4 current speed is related to the v velocity component (r^2 = 0.78) while the current direction links to u and w velocity components (r^2 = 0.55 and r^2 = 0.40, respectively). In addition to Set 1 and 4, Set 2 and 3 were also evaluated with correlation analysis and we found similarly that waves, wind, tide, and currents are unrelated to turbulence parameters. Although we found a significant correlation between tide and current direction and between tide and u velocity component on Set 2 (r^2 = 0.69 and r^2 = 0.60, respectively) and correlation among current direction and u velocity component also on Set 2 (r^2 = 0.56). In Set 3, There are correlations between current direction and u velocity component (r^2 = 0.59), and between the v and w velocity components (r^2 = 0.63). In this context, even if no tide and current correlation exist with turbulence on these sets the difference in current interactions and a change in momentum transfer during neap tides and spring tides could be linked to the tide effect on turbulence parameters during the ebb and flood tides. This will be evaluated in the TKE budget subsection.

3.2.2. Turbulent kinetic energy budget

The rate of change of TKE to time, in the mean flow, can be approximated to the local production–dissipation balance such as

$$\frac{\partial \langle k \rangle}{\partial t} \approx P - \epsilon, \tag{22}$$

after neglecting the buoyancy and the self-advection terms (Guerra and Thomson, 2017; Trowbridge and Elgar, 2001; Craig and Banner, 1994). As previously mentioned, the inertial dissipation method, or IDM, gives more reliable values of ϵ than those obtained with the SFM (Guerra and Thomson, 2017; Thiébaut et al., 2020b). So here we used IDM to evaluate ϵ. It is a common practice to study the TKE budget in environments characterized by strong tidal currents, with speeds >3 m s^{-1}, or with some tidal orbital influence on turbulence (McMillan et al., 2016; Williams and Simpson, 2004).

In contrast, our study area is a mesotidal bay with a tidal range of ~2.2 m with moderate tidal currents (up to 0.35 m s^{-1}) and some wave effect on the TKE intensification, as confirmed in the previous sections. Considering this low energy system, we decided to test the combined effect of tides (spring-neap tides) and waves on the TKE balance between P and ϵ by selecting four different conditions during periods of 36 h (see Table 3). First, we identified the periods of spring tides or ST (yeardays 90–98 and 105–112) and neap tides or NT (yeardays 85–89, 99–104, and 113–114), and then we identified the periods of relevant wave presence (H_s > 1.3 m on ST and H_s > 0.7 m on NT) and wave absence (H_s < 1.16 m on ST and H_s < 0.7 m on NT). These data sets were numbered one to four (see Fig. 7). Set 1 and Set 2 correspond to NT under strong and medium conditions, respectively (Set 1: yeardays 99–10; Set 2: yeardays 86–88). Similarly, Set 3 and Set 4 correspond to ST under medium and weak wave conditions, respectively (Set 3: yeardays 107–109; Set 4: yeardays 92–94).

Hourly vertical changes throughout the observation of P and ϵ for each Set of 36 h are given in Fig. 9a-d and Fig. 10a-d. The figures display several contrasting features between both turbulence metrics. Of note here are the negative P estimates which correspond to white gaps in the P plots, and are commonly associated with periods of slack water. Other sources of negative P are sidelobe contamination near the sea surface, statistical non-homogeneity of b_i over the variance computation period, statistical non-homogeneity of u, v, and w over the distance between beams, frequent values below the noise floor, surface or internal wave bias, and ADCP motion (Osalusi et al., 2009a; Lu and Lueck, 1999b). We can discard side-lobe contamination, wave bias, and ADCP motion because these issues were addressed during our ADCP data preprocessing. However, statistical non-homogeneity in beam variance computation and estimation of u, v, and w, where frequent values below the noise floor could be associated with negative estimates of P. Based on this, we exclude negative values to show how P and η associate with slack water periods when the reduced mean flow restrains P. Discussion of these sources of error and their link to velocity and turbulence calculations will be presented in Section 3.3.

Another feature, the balance between ϵ and P, is commonly studied in highly energetic systems with both turbulence metrics tracking each other and displaying a clear tidal variation. Our results indicate that ϵ is not only much greater than P, but also indicate an unclear association with the ebb and flood tide in any of the 36 hr data sets. Thibaut2020 found an imbalance between ϵ and P during periods of low tidal velocity (< 1 m s^{-1}), with a reduced gap between these turbulence metrics during peak tidal flow, with tidal velocities reaching up to 3.5 m s^{-1} in Alderney Race, a highly energetic tidal channel. Our results with low TKE P rates are the consequence of testing a low energy environment, a mesotidal bay, with tidal currents just up to 0.17 m s^{-1} in the four 36 hr data sets as shown in Table 3.

We previously mentioned that waves have some enhancement effect on TKE and by comparison, the data sets with waves present (Sets 1 and 3) display greater values of P and ϵ than in the sets without waves present. Furthermore, when we compare the tidal effect, the NT data

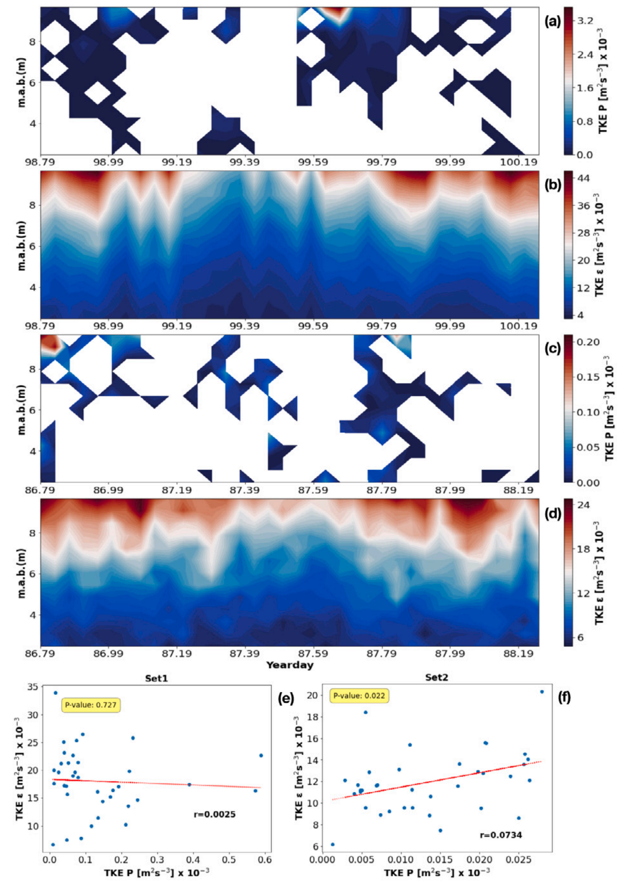

Fig. 9. Time-depth diagrams of TKE P and TKE ϵ over a 36-h period. (a) Production and (b) Dissipation Set 1: strong waves and neap tide conditions, on yeardays 99–101. (c) Production and (d) Dissipation Set 2: medium wave and neap tide conditions, on yeardays 86–88. (e) Production vs Dissipation Set 1. (f) Production vs Dissipation Set 2. Of note here are the negative P estimates which correspond to white gaps in the P plots, and are commonly associated with periods of slack water.

Table 3
Turbulent kinetic energy production rate (P) and Turbulent kinetic energy dissipation rate (ϵ) evaluated under different wave and tide conditions.

	Neap tide	
	Set 1 (99 – 101) *yeardays* *Strong Waves*	Set 2 (86 – 88) *yeardays* *Medium Waves*
P (10^{-5} m^2 s^{-3})	3.7–59	1–5.4
P (log_{10} m^2 s^{-3})	$10^{-4.4}$–$10^{-3.2}$	10^{-5}–$10^{-4.2}$
ϵ (10^{-3} m^2 s^{-3})	5.7–32.5	6.1–19.9
ϵ (log_{10} m^2 s^{-3})	$10^{-2.2}$–$10^{-1.5}$	$10^{-2.2}$–$10^{-1.7}$
H_s (m)	1.3–2.24	0.66–1.16
Flow speed (10^{-2} m s^{-1})	2.7–14.1	1.3–15.4
η (m)	−0.70–0.69	−0.66-0.41
	Spring tide	
	Set 3 (107 – 109) *yeardays* *Medium Waves*	Set 4 (92 – 94) *yeardays* *Weak Waves*
P (10^{-5} m^2 s^{-3})	1-6.5	0.6–2.8
P (log_{10} m^2 s^{-3})	10^{-5}–$10^{-4.1}$	$10^{-5.2}$–$10^{-4.5}$
ϵ (10^{-3} m^2 s^{-3})	6.2–22.9	5.9–12.8
ϵ (log_{10} m^2 s^{-3})	$10^{-2.2}$–$10^{-1.6}$	$10^{-2.2}$–$10^{-1.9}$
H_s (m)	0.67–1.14	0.43–0.79
Flow speed (10^{-2} m s^{-1})	2.4–14.5	5.2–17.2
η (m)	−0.92–0.98	−0.74-0.69

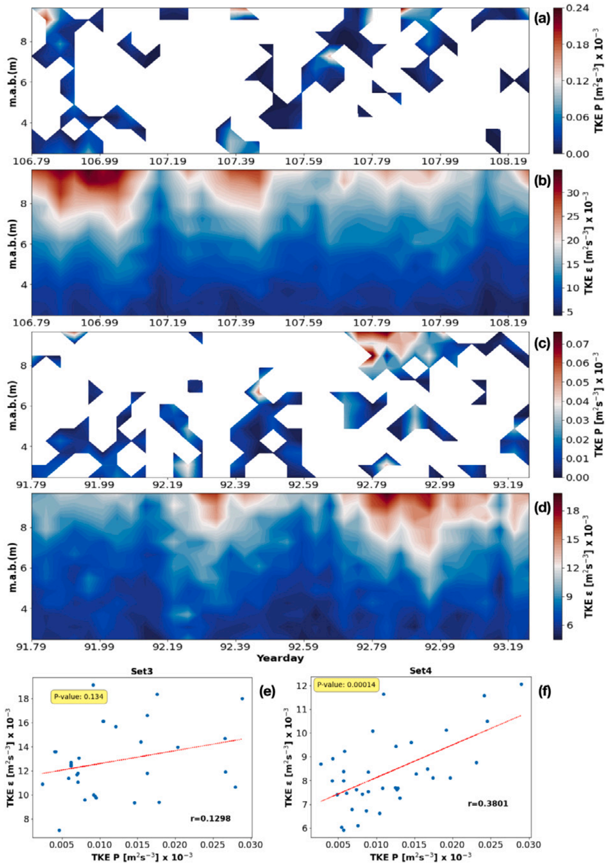

Fig. 10. Time-depth diagrams of TKE P and TKE ϵ over a 36-h period. (a) Production and (b) Dissipation Set 3: medium wave and spring tide conditions, on yeardays 107–109. (c) Production and (d) Dissipation Set 4: weak wave and spring tide conditions, on yeardays 92–94. (e) Production vs Dissipation Set 3. (f) Production vs Dissipation Set 4. Of note here are the negative P estimates which correspond to white gaps in the P plots, and are commonly associated with periods of slack water.

sets display greater values of P and ϵ than the ST data sets, as can be seen in Table 3. Tidal current velocities are quite similar, ranging from 1.3 to 17.2 cm s^{-1} in all data sets, with slightly faster currents in Set 4 (see Table 3). In addition, η displays a similar tendency with the largest fluctuations in ST. As previously mentioned, some researchers have selected data ranges where significant wave height (Hs) is relatively small (H_s < 1 m) to estimate turbulence parameters (Serio and Mossa, 2015; Thiébaut et al., 2020b), under the assumption that wave-induced variability is reduced and turbulence structure becomes more stable. In our case, the smallest Hs range was recorded during Set 4 (0.43 to 0.79 m). This range reflects conditions where waves are present but moderate-sufficient to influence turbulence without introducing extreme variability. Therefore, we interpret this range (H_s < 1 m 0.79 m) as optimal for evaluating turbulence under the influence of waves while minimizing complicating factors such as breaking and strong nonlinearity. This proposed cut-off for H_s is supported by a comparison between P and ϵ time-depth diagrams. In Set 4, P and ϵ surface maxima between yeardays 93.7 to 94.0 (see Fig. 10c–d,f) show some correspondence between these turbulence metrics which are absent in the other 36-h sets (see Figs. 9a–b,e, 9c–d,f and 10a–b,e).

In addition, a correlation analysis between P and ϵ shows that the largest significant correlation (r= 0.38, pvalue < 0.01) corresponds to Set 4 (see Fig. 10f). Each of the four 36-hour sets, representing different wave and tide conditions, exhibits distinct levels of uncertainty across the analysed parameters. For example, Set 1 consistently showed the highest levels of Doppler noise and the largest associated uncertainties across most turbulence variables and the lowest correlation of all sets (see Figs. 9e, 9f and 10e) between P and ϵ (r= 0.0025, pvalue > 0.01). In contrast, Set 4 exhibited the lowest levels of Doppler noise and the smallest uncertainties (see Section 3.3). This pattern is evident across all four 36 h sets examined. The improved data quality in Set 4 (see Section 3.3) helps to explain the stronger correlation observed between P and ϵ in this period. The reduced background noise improves the reliability of the turbulence estimates, supporting a more consistent interpretation of energy dynamics under the prevailing oceanographic conditions.

An evaluation of the balance between P and ϵ is not as straightforward as one may think. First, we must consider the clear energy difference in the tidal flow of our study area compared to more energetic environments such as tidal channels, bays, estuaries, and coastal lagoons (Lu and Lueck, 1999b; Rippeth et al., 2002; Nystrom et al., 2007; Burchard et al., 2008; Kirincich and Rosman, 2011; Serio and Mossa, 2015). A strong tidal flow of up to 4 m s^{-1} can be found in tidal channels (Osalusi et al., 2009b), while moderated tidal flows of up to 0.85 m s^{-1} can be found in some bays with moderate wave effect (Wiles et al., 2006; Souza and Howarth, 2005). In moderate tidal flow environments the P rate ranges from 10^{-3} to 10^{-1} m^2 s^{-3} (Wiles et al., 2006; Dewey and Crawford, 1988), while in more energetic environments the range is $10^{-8.7}$ to $10^{-0.5}$ m^2 s^{-3} (Souza and Howarth, 2005; Rippeth et al., 2002; Osalusi et al., 2009a). In our study area, the time-depth diagrams of P have lower intensities near the bottom, increasing toward the surface. Such distribution follows the time-depth diagrams of TKE and Reynolds stresses. The TKE P mean range from ~2.47 mab to ~9.67 mab correspond $10^{-5.2}$ to $10^{-3.2}$ m^2 s^{-3} (0.6 to 59 × 10^{-5} m^2 s^{-3}). The TKE P time-depth diagram range from 10^{-6} to $10^{-2.46}$ m^2 s^{-3} (0.1 to 346 × 10^{-5} m^2 s^{-3}). This range of P is valid for all four sets, which have differences as previously described, but in general, our P data fall within the expected data range of other studies with similar tidal currents and wave conditions (Guerra and Thomson, 2017; Rippeth et al., 2002; Lu and Lueck, 1999b; Rippeth et al., 2003).

Regarding ϵ, in moderate tidal flow environments, ϵ ranges from 10^{-4} to 10^{-1} m^2 s^{-3} (Wiles et al., 2006; Dewey and Crawford, 1988), while in more energetic environments the ϵ range is $10^{-2.4}$ to $10^{-0.3}$ m^2 s^{-3} (Rippeth et al., 2002; Osalusi et al., 2009a). The TKE ϵ time-depth diagram have low intensities near the bottom, increasing toward the surface. This distribution follows the time-depth diagrams of TKE and Reynolds stresses. The TKE ϵ mean range from ~2.47 mab to ~9.67 mab corresponds with $10^{-2.24}$ to $10^{-1.48}$ m^2 s^{-3} (5.7 to 32.5 × 10^{-3} m^2 s^{-3}). The TKE ϵ time-depth diagram range from $10^{-2.4}$ to $10^{-1.33}$ m^2 s^{-3} (4 to 46 × 10^{-3} m^2 s^{-3}). This range of TKE ϵ includes all four data sets, which have differences as previously described, but, in general, our TKE ϵ data fall within the expected data range of other studies (Wiles et al., 2006; Dewey and Crawford, 1988; Osalusi et al., 2009b).

Orton et al. (2010) studied the tidal and atmospheric influences on turbulence at the Hudson River estuary and found that wind is the primary driver of turbulence, while ϵ has a positive correlation with surface water speed as well as net upward air-sea heat flux. More shear stress is observed during ebb than during flood, leading to an increase in the magnitude of P and ϵ during ebb flow. In such study, P and ϵ range from 10^{-6} to $10^{-4.5}$ m^2 s^{-3} (1 to 31 × 10^{-6} m^2 s^{-3}) and 10^{-7} to $10^{-4.8}$ m^2 s^{-3} (0.1 to 10 × 10^{-6} m^2 s^{-3}), respectively. Simpson et al. (2005) studied the impact of tidal straining on the cycle of turbulence at the York River estuary in the presence of stratification comparing NT and ST conditions. They found that during stratification, P is mainly constrained to the mixed layer below the homogeneous stratified layer during neap tides, but P is enhanced during spring tides, normally with stronger dissipation rates during ebb. In such work, P rate range from 10^{-4} to 10^{-1} m^2 s^{-3} (0.1 to 100 × 10^{-3} m^2 s^{-3}) on neap tides and 0 to 0.1 m^2 s^{-3} on spring tides, respectively.

The previous results help us to put in context our results for P and ϵ rates. For example, in the case of P we can note that the range of data of P shown on Table 3 ($10^{-5.2}$ to $10^{-3.2}$ m^2 s^{-3}) and the previously presented TKE P data agree with P reported by Orton et al. (2010), Simpson et al. (2005) and to some extent it also agrees with the data range found at Alderney race by Thibaut2020. Our TKE production data agree with that of a low energetic flow environment. For the case of ϵ, our data range ($10^{-2.2}$ to $10^{-1.6}$ m^2 s^{-3}) corresponds to rates greater than those found by Orton et al. (2010) on the Hudson river estuary, and similar in range to those found by Thibaut2020 on Alderney race. Our data range for ϵ corresponds to the upper end of the data range for environments with a moderate tidal flow (Dewey and Crawford, 1988; Wiles et al., 2006). These results suggest that TSB, a mesotidal bay, is a tidal environment with a flow that falls in the transition between moderate to high energetic tidal flow. The following section will present a more detailed description of how tidal flows affect turbulence.

3.2.3. Mean flow, waves, and turbulence characteristics during flood and ebb tides

Table 4 shows mean flow velocity component magnitudes, the TKE, the shear components of the Reynolds stress, production rate, dissipation rate and averaged wave parameters, for Sets 1 to 4, for flood and ebb tide phases. One important thing to remember is the myriad of processes that can affect turbulence in near-shore environments such as estuaries, coastal lagoons, and the surfing area in the coastal zone. Wind shear stress, tidal current shear stress, wave breaking, and heat fluxes are some of the main mechanisms that enhance near-surface turbulence but only heat fluxes due to evaporation and stratification affect buoyancy (convection) (Orton et al., 2010). In the nearshore area, we can discard TKE fluxes generated by buoyancy because our sampling was performed in a mixed water column and no stratification is observed during strong wind and wave season (Trowbridge and Elgar, 2001; Craig and Banner, 1994). Boundary layer processes during water mixing also are absent on the nearshore sampling site. However, our work shows that even with the applied data preprocessing protocol and the tidal signal filtering, we are still able to detect the wave effect on turbulence parameters.

To evaluate the difference in turbulence characteristics during flood and ebb tide, we focused our attention on our four 36-hour sets where Set 1 and Set 2 correspond to NT under strong and medium conditions, respectively (Set 1: yeardays 99–10; Set 2: yeardays 86–88). Similarly, Set 3 and Set 4 correspond to ST under medium and weak wave conditions, respectively (Set 3: yeardays 107–109; Set 4: yeardays 92–94). It is worth pointing out that the wave conditions are very similar for Sets 2 and 3, so we can check for differences associated with neap and spring tides with these two sets. In the case of the speed component u, we only observe a difference between flood and ebb tides for Set 1, when waves are strong. u is the zonal speed and therefore approximately perpendicular to the coast, thus it is expected that the waves, which also move perpendicular to the coast, will affect the currents, and that there will be differences between flood and ebb tides. There are significant differences in v between flood and ebb tides in the periods corresponding to neap tides, i.e. for Sets 1 and 2, but tidal asymmetry effects on v are very small during spring tides.

We observed that there is a noticeable difference in P during flood and ebb tides for Set 2, but for Set 3 there is no tidal asymmetry. The same applied to ϵ, but the difference between flood and ebb for Set 2 is not that large (2.6×10^{-3} m^2 s^{-3}). Bear in mind that throughout the observation period, ϵ is two orders of magnitude larger than P.

Another similarity to note is that all parameters increase in magnitude from bottom to surface, we chose three different depths to evaluate the vertical structure of all parameters (2.47, 5.47, and 8.47 m) and found this common feature in all mean flow and turbulent flow variables. Therefore, turbulence increases from bottom to surface in close relationship with the current velocity profile.

Now the last similarity is in the context of TKE and Reynolds shear stresses. All these parameters have not only similar magnitudes from Set 1 to Set 4 but also display a symmetric effect during flood and ebb flow meaning that there is an equilibrium in these turbulence parameters without tide phase effect or tide flow cycle. TKE values range from 8.9 to 12×10^{-3} m^2 s^{-2} while shear stresses $\overline{u'w'}$ and $\overline{v'w'}$ values range from -0.9 to -1.4×10^{-3} m^2 s^{-2} and 0.81 to 1.1×10^{-3} m^2 s^{-2}, respectively (see Table 4).

Table 4
Depth-integrated mean flow, turbulence characteristics, TKE budget parameters and mean spectral wave parameters, for Sets 1–4 and flood and ebb tides. NT: Neap tides; ST: Spring tides; SW: Strong Waves; MW: Medium Waves; WW: Weak Waves.

	Neap tide			
	Set 1: NT, SW		Set 2: NT, MW	
	Flood	*Ebb*	*Flood*	*Ebb*
u (10^{-2} m s^{-1})	−0.5	−1.7	−4.8	−4.3
v (10^{-2} m s^{-1})	2.5	−17	−7.7	−3.9
w (10^{-3} m s^{-1})	−2	−2.7	−2	−1.8
$\overline{TKE}$ (10^{-3} m^2 s^{-2})	10	12	10	10.2
$\overline{u'w'}$ (10^{-3} m^2 s^{-2})	−1.3	−1	−0.9	−1.4
$\overline{v'w'}$ (10^{-3} m^2 s^{-2})	0.86	1.1	0.93	0.94
P (10^{-6} m^2 s^{-3})	2.11	9.86	6.2	1.61
ϵ (10^{-3} m^2 s^{-3})	18	12	12.5	9.9
H_s (m)	1.71	2.02	0.953	0.734
T_p (s)	8.8	10.7	12.2	11.6
D_p (°)	261	259	264	254
	Spring tide			
	Set 3: ST, MW		Set 4: ST, WW	
	Flood	*Ebb*	*Flood*	*Ebb*
u (10^{-2} m s^{-1})	−5	−4.5	−5.7	−6.1
v (10^{-2} m s^{-1})	14.6	14	1.2	1
w (10^{-3} m s^{-1})	−0.8	−0.9	−1.7	−1.6
$\overline{TKE}$ (10^{-3} m^2 s^{-2})	10.5	11	9.4	8.9
$\overline{u'w'}$ (10^{-3} m^2 s^{-2})	−1.1	−1	−1	−1.1
$\overline{v'w'}$ (10^{-3} m^2 s^{-2})	0.96	1	0.87	0.81
P (10^{-6} m^2 s^{-3})	2.26	2.61	2.66	1.86
ϵ (10^{-3} m^2 s^{-3})	13.4	12.6	8.2	8.9
H_s (m)	0.845	0.755	0.536	0.599
T_p (s)	10.6	11.5	11.8	13.3
D_p (°)	260	257	256	248

Regarding mean flow parameters, we can identify relevant differences in the case of velocity components u, v, and w. The magnitude of the meridional velocity component v is more notable than the zonal velocity component u so we will discuss the most relevant of them first.

The meridional v component besides being predominant in the context of velocity magnitude for all sets also has the greatest differences in flood and ebb flow, mainly during NT. If we take a close look at Set 1 with strong wave conditions, the asymmetry is dominated by ebb flow with the largest difference in all sets (14.5×10^{-2} m s^{-1}) (see Table 4). In the case of medium wave conditions on NT and ST, we can notice that the largest asymmetry between flood and ebb flow (3.8×10^{-2} m s^{-1}) corresponds to Set 2 (NT-MW) (see Table 4). In contrast during ST (Set 3), there is a magnification of the v magnitude component of almost a factor of two concerning Set 2, but with symmetry between flood and ebb flow effect on the v velocity component. During weak waves (Set 4) we not only found the smallest values of v but also little differences between flood and ebb (0.2×10^{-2} m s^{-1}). In summary, it is clear that in the turbulent flow field, there is no effect of the flood-ebb cycle, but on the mean flow field not only its effect is evident on all velocity components but mainly on the predominant meridional v velocity, with other noticeable differences for NT and ST.

In the case of the u component we can notice that the Set 1 (NT-SW) u has the smallest magnitude of all sets, but the asymmetry in velocity magnitude (1.2×10^{-2} m s^{-1}) is the largest one, with the magnitude of u being three times larger during ebb than during flood tides (see Table 4). On the rest of the sets, we can appreciate there is symmetry between flood and ebb flow in u magnitudes, but if we compare NT and ST on medium wave conditions (Sets 2 and 3) there is no clear difference in u

magnitudes. If we even compare with Set 4, with weak waves, although the magnitude is slightly greater the asymmetry between flood and ebb flow is quite small (0.5×10^{-2} m s^{-1}) (see Table 4).

The w velocity component is larger during NT (Sets 1 and 2) than during ST (Sets 3 and 4) with the biggest difference between flood and ebb under NT and strong waves (SW). In the case of medium wave conditions (Sets 2 and 3), it is evident that w is larger during NT than during ST. However, w is large during ST and weak waves (see Table 4).

Even if it appears that there is no direct effect of tide on turbulence based on the turbulent flow field results and the correlation analyses, a comparison of P and ϵ allows us to discriminate important differences. In the case of P, we can note the difference in magnitude during NT and ST (see Table 4). Another important difference is that under strong wave conditions (Set 1) the asymmetry is the greatest when compared with other Sets (7.75×10^{-3} m^2 s^{-3}) and is enhanced by the ebb flow. The second largest value of P corresponds to medium wave conditions on NT (Set 2), not only is the second largest asymmetry found on all sets (4.59×10^{-3} m^2 s^{-3}), but also is dominated by flood flow.

A comparison between NT and ST during medium wave conditions shows that in NT there is more production of TKE and asymmetry than in ST under these medium wave conditions. Besides on ST, there is a clear symmetry between flood and ebb flow in P. In contrast, with weak waves (Set 4) and ST we can note that even if the asymmetry between flood and ebb flood is not of the same magnitude as on NT, the flood flow enhances P rate. The observed pattern on NT for P is quite similar to the pattern described for the meridional velocity component indicating the relationship between P and u,v,w components, as the gradient of velocities concerning depth is used to calculate P.

In the case of the TKE dissipation rate ϵ, there is a clear difference in ϵ magnitude between NT and ST. Another important difference, in ϵ, is that under strong wave conditions (Set 1) the ϵ asymmetry is the greatest when compared with other sets (6×10^{-3} m^2 s^{-3}) and is enhanced by flood flow (see Table 4). One of the largest values of TKE ϵ corresponds to medium wave conditions on NT (Set 2), not only is one of the largest asymmetries found on all sets (2.6×10^{-3} m^2 s^{-3}), but also is dominated by flood flow. A comparison between NT and ST (Sets 2 and 3) during medium wave conditions shows that in NT there is more dissipation asymmetry than in ST under these medium wave conditions (0.8×10^{-3} m^2 s^{-3}) (see Table 4). Besides on ST, there is slightly more asymmetry with flood flow on TKE ϵ and the magnitude of asymmetry is quite similar to the NT (Set 2). In contrast, with weak waves and ST (Set 4), we can note that the asymmetry between flood and ebb flood is of the same magnitude as on medium wave condition on ST, the ebb flow enhances ϵ. It is clear that the effect of flood flow on ϵ is related to the presence of strong waves (Set 1), and medium wave conditions (Sets 2 and 3). This pattern is the opposite of that of weak waves, with an asymmetric effect on ϵ during ST.

3.3. Error analysis

The TKE budget was discussed in Section 3.2.2. Some possible sources of error are associated with the white gaps in the TKE P time series and negative estimates of TKE P. Statistical non-homogeneity in beam variance computation and estimation of u, v, and w, with frequent values below the noise floor could be associated with negative estimates of P. Several studies confirmed that ADCP white noise is affected by the intensification of waves and currents during instrument deployment (Terray et al., 1999; Zedel, 2001; Shcherbina and D'Asaro, 2024) resulting in variability of Doppler noise along a single installation.

The uncertainties associated with velocity (σ_N^2), TKE (σ_{TKE}^2), shear stress (σ_S^2), Reynolds stress (σ_R^2), TKE P (σ_P^2), and TKE ϵ (σ_ϵ^2) calculations were estimated following the approach of Williams and Simpson equations (2004) (Williams and Simpson, 2004). As summarized in Table 5, each of the four 36 h sets, corresponding to different wave and tidal conditions, displayed distinct levels of uncertainty for the calculated parameters.

Table 5
Uncertainties of the along beam velocity (σ_N^2), the TKE (σ_{TKE}^2), the shear stress (σ_S^2), the Reynolds stress (σ_R^2), the rate of production (σ_P^2), and the rate of dissipation (σ_ϵ^2).

	Set 1	Set 2	Set 3	Set 4
σ_N^2 (10^{-2} m s^{-1})	4.45	2.45	2.99	1.96
σ_{TKE}^2 (10^{-3} m^2 s^{-2})	1.98	0.59	0.89	0.38
σ_S^2 (10^{-4} m^2 s^{-2})	5.99	3.29	4.02	2.64
σ_R^2 (10^{-4} m^2 s^{-2})	1.05	0.31	0.47	0.20
σ_P^2 (10^{-4} m^2 s^{-3})	4.34	1.77	2.38	1.27
σ_ϵ^2 (10^{-5} m^2 s^{-3})	3.24	1.21	1.43	0.21

Set 1 exhibited the highest Doppler noise levels, resulting in the largest uncertainties across most turbulence estimates. In contrast, Set 4 consistently showed the lowest uncertainties, reflecting more stable measurement conditions. This reduction in noise likely contributes to the improved correlation observed between TKE production and dissipation in Set 4 respect to the other 36 h sets (Set1, Set2, and Set3) as previously mentioned in Section 3.2.2. The enhanced data quality during this period enables a more robust assessment of turbulence energetics under varying forcing conditions.

In general, we observed important differences between the four sets of waves and tide conditions in Sets 1 to 4, and Set 4 has the lowest noise for all calculations, hence the better correlation between TKE P and TKE ϵ for Set 4, associated with a lower noise background.

Our work aimed to describe the vertical structure of turbulence in TSB, a mesotidal bay in the Mexican Pacific. As we confirm that local wind and local waves are linked, we also found that the wave interaction in our turbulence parameters is important during strong wave events when $H_s > 0.75$ m. We applied the variance method to obtain turbulence metrics such as Reynolds stresses, TKE, and anisotropy, followed by an evaluation of the TKE budget. We also compared mean flows, waves and turbulence characteristics during flood and ebb tides for the four sets. Finally, an evaluation of the errors for these four 36-h sets shows that ADCP deployments are affected by extreme conditions and that error estimates and corrections should be considered carefully.

4. Conclusions

Turbulence characterization in coastal and estuarine environments is crucial for several applications, in particular for wave and current energy conversion. This study is based on measurements obtained between March 26, 2019, and April 24, 2019, with a five-beam ADCP deployed in TSB, a mesotidal bay in the NorthWest of the Baja California Peninsula, to analyse the Reynolds Stress shear components, the TKE, the anisotropy ratio, and the TKE energy budget differences between flood and ebb tides, with particular emphasis on four tidal and wave conditions: neap tides and strong waves, neap tides and medium waves, spring tides and medium waves, spring tides and weak waves. The four scenarios were characterized by mean flow and spectral wave characteristics. We also observed from the waverose diagrams and wind measurements, that local waves were generated by winds blowing on the TSB, strengthening the significant wave heights. Swell waves entered TSB predominantly from the West. Tidal decomposition analysis of surface elevation and current data confirmed that the tidal signature is that of a mixed, predominantly semi-diurnal tide, but non-linear effects of the M2, S2 and K1 components also have an influence on the flow. From time-depth diagrams of current speed, we concluded that the current speed increases from the bottom to the surface.

The analysis of the Reynolds stresses shear components and the TKE showed that $\overline{u'w'}$ and TKE tend to increase from the bottom to the surface, while $\overline{v'w'}$ increases from surface to bottom. Our study confirms that waves affect turbulence since we observed an intensification of turbulent processes during neap tides and strong wave conditions.

TKE production was also larger under neap tides and strong wave conditions than in the other three tide and wave scenarios. The TKE dissipation rate minima were almost the same in all cases, but the maxima did depend on the wave and tide conditions, with the largest values under strong waves and the smallest values under weak waves. Throughout the observation period, we also observed that the TKE dissipation rate is two orders of magnitude larger than the TKE production rate. This predominance of dissipation concerning production is commonly found in low-energy systems, such as estuaries or semi-enclosed bays. Our findings indicate that a great deal of the TKE transferred by the mean flow is rapidly dissipated, throughout the water column.

A study separating flood and ebb tides showed that the differences in turbulence characteristics during flood and ebb tides at the TSB are very small. Tidal asymmetry is more noticeable during neap tides, and more so during strong than during medium wave conditions. The same is true for the Reynolds stress shear components. Finally, the asymmetry between flood and ebb tides on production and dissipation rates is only noticeable during neap tides and strong wave conditions.

Many of the works have focused on more energetic sites as tidal channels or inlets (Simpson et al., 2005; Orton et al., 2010; Lu and Lueck, 1999b; Stacey et al., 1999; Thiébaut et al., 2020c) but the characterization of turbulence in mesotidal bays is limited (Serio and Mossa, 2015) and our work fills the gap of information of turbulence vertical structure on low energy sites and the effects of waves and tides on turbulence. In addition, even though five-beam ADCPs are commercially accessible very few studies have tried to reevaluate the previous assumption of turbulence anisotropy to calculate TKE density with four-beam ADCPs. Such an assumption generates a bias because as we have shown anisotropy displays a vertical structure that changes with time along TKE and Reynolds stresses. Something that was not previously discussed or presented due to the lack of a vertical beam to directly estimate anisotropy and TKE. In addition, our research highlights the dissipative nature of mesotidal bays, but also shows that strong waves and neap tide conditions enhance turbulence in the water column.

Future work will focus on turbulence characterization under more energetic flow conditions, such as in the canyon at the Southern side of the TSB, where the currents are accelerated by Venturi effects, to see if and when waves still have an effect on turbulence under stronger current conditions. Other sites where this flow acceleration occurs can be found in the Great Island Region of the Gulf of California.

CRediT authorship contribution statement

Victor A. Arias-Esquivel: Writing – original draft, Data curation. **Victor M. Godínez:** Writing – original draft, Data curation. **Markus Gross:** Writing – original draft, Data curation, Conceptualization. **Anahí Bermúdez-Romero:** Data curation. **Vanesa Magar:** Writing – original draft, Funding acquisition, Data curation, Conceptualization.

Declaration of competing interest

The authors declare that they have no known competing financial interests or personal relationships that could have appeared to influence the work reported in this paper.

Acknowledgements

This work was partly supported through project no. 249795, Call 2014-06 by the CONACYT's Energy Sustainability Call 2014-06 of Proposals for the "Centro Mexicano de Inovación de Energías del Océano" (CEMIE-OCEANO,2017–2022), partly through a postdoctoral scholarship to the first author by CONACYT (grant 81593,2021–2023), and partly through internal projects by CICESE (2014 to date). We want to thank Marinna Martini from NOAA for sharing codes, advice on data processing, and comments on a previous version of the manuscript.

Data availability

Data will be made available on request.

References

Abdessalem, B., John, H., Antonella, C., Johanning, L., 2013. Characterising turbulence from a 5-beam ADCP when optimised for wave measurements.

Agrawal, Y.C., Terray, E.A., Donelan, M.A., Hwang, P.A., Williams, A.J., Drennan, W.M., Kahma, K.K., Krtaigorodskii, S.A., 1992. Enhanced dissipation of kinetic energy beneath surface waves. Nature 359 (6392), 219–220. http://dx.doi.org/10.1038/359219a0.

Alvarez-Sánchez, L., 1977. Vientos en la Bahía de Todos Santos, Baja California. Cienc. Mar. 4 (1), 81–88. http://dx.doi.org/10.7773/cm.v4i1.301.

Alvarez-Sánchez, L., Hernández-Walls, R., Durazo-Arvizu, R., 1988. Drift patterns of Lagrangian tracers in Todos Santos Bay. Cienc. Mar. 14 (4), 135–162. http://dx.doi.org/10.7773/cm.v14i4.609.

Bowden, K.F., Fairbairn, L.A., 1952a. A determination of the frictional forces in a tidal current. Proc. R. Soc. Lond. Ser. A. Math. Phys. Sci. 214 (1118), 371–392. http://dx.doi.org/10.1098/rspa.1952.0175.

Bowden, K.F., Fairbairn, L.A., 1952b. Further observations of the turbulent fluctuations in a tidal current. Philos. Trans. R. Soc. Lond. Ser. A, Math. Phys. Sci. 244 (883), 335–356. http://dx.doi.org/10.1098/rsta.1952.0008.

Bowden, K.F., Fairbairn, L.A., 1956. Measurements of turbulent fluctuations and Reynolds stresses in a tidal current. Proc. R. Soc. Lond. Ser. A. Math. Phys. Sci. 237 (1210), 422–438. http://dx.doi.org/10.1098/rspa.1956.0188.

Burchard, H., Craig, P.D., Gemmrich, J.R., van Haren, H., Mathieu, P.-P., Meier, H.M., Smith, W.A.M.N., Prandke, H., Rippeth, T.P., Skyllingstad, E.D., Smyth, W.D., Welsh, D.J., Wijesekera, H.W., 2008. Observational and numerical modeling methods for quantifying coastal ocean turbulence and mixing. Prog. Oceanogr. 76 (4), 399–442. http://dx.doi.org/10.1016/j.pocean.2007.09.005.

Calvino, C., Bennis, A.-C., Furgerot, L., Pascal, B.d.B., Emmanuel, P., 2023a. Estimation and characterisation of the wave-induced turbulent kinetic energy and turbulent dissipation from ADCP data. Proc. Eur. Wave Tidal Energy Conf. 15, http://dx.doi.org/10.36688/ewtec-2023-299.

Calvino, C., Furgerot, L., Poizot, E., du Bois, P.B., Bennis, A.-C., 2023b. Model and method to predict the turbulent kinetic energy induced by tidal currents, application to the wave-induced turbulence. Renew. Energy 216, 119024. http://dx.doi.org/10.1016/j.renene.2023.119024.

Craig, P.D., Banner, M.L., 1994. Modeling wave-enhanced turbulence in the ocean surface layer. J. Phys. Oceanogr. 24 (12), 2546–2559. http://dx.doi.org/10.1175/1520-0485(1994)024<2546:mwetit>2.0.co;2.

Defant, A., 1961. Physical Oceanography, vol. 1, Pergamon.

Dewey, R.K., Crawford, W.R., 1988. Bottom stress estimates from vertical dissipation rate profiles on the continental shelf. J. Phys. Oceanogr. 18 (8), 1167–1177. http://dx.doi.org/10.1175/1520-0485(1988)018<1167:bsefvd>2.0.co;2.

Dewey, R., Stringer, S., 2017. http://dx.doi.org/10.13140/RG.2.1.1042.8002, Unpublished, URL: http://rgdoi.net/10.13140/RG.2.1.1042.8002.

Drennan, W.M., Donelan, M.A., Terray, E.A., Katsaros, K.B., 1996. Oceanic turbulence dissipation measurements in SWADE. J. Phys. Oceanogr. 26 (5), 808–815. http://dx.doi.org/10.1175/1520-0485(1996)026<0808:otdmis>2.0.co;2.

Dronkers, J., 1964. Tidal Computations in Rivers and Coastal Waters. North-Holland Publishing Company, URL: https://books.google.com.mx/books?id=Ro9RAAAAMAAJ.

Durazo, R., Flores-Vidal, X., Castro, R., Ocampo-Torres, F.J., Saavedra, J., Rodríguez-Padilla, I., Larrañaga, M., 2024. Surface circulation in Todos Santos Bay, Baja California, México. Cont. Shelf Res. 273, 105171. http://dx.doi.org/10.1016/j.csr.2024.105171.

Durgesh, V., Thomson, J., Richmond, M.C., Polagye, B.L., 2014. Noise correction of turbulent spectra obtained from acoustic doppler velocimeters. Flow Meas. Instrum. 37, 29–41. http://dx.doi.org/10.1016/j.flowmeasinst.2014.03.001.

Feddersen, F., Trowbridge, J.H., 2005. The effect of wave breaking on surf-zone turbulence and alongshore currents: A modeling study*. J. Phys. Oceanogr. 35 (11), 2187–2203. http://dx.doi.org/10.1175/jpo2800.1.

Feddersen, F., Trowbridge, J.H., Williams, A.J., 2007. Vertical structure of dissipation in the nearshore. J. Phys. Oceanogr. 37 (7), 1764–1777. http://dx.doi.org/10.1175/jpo3098.1.

Fisher, A.W., Sanford, L.P., Scully, M.E., 2018. Wind-wave effects on estuarine turbulence: A comparison of observations and second-moment closure predictions. J. Phys. Oceanogr. 48 (4), 905–923. http://dx.doi.org/10.1175/jpo-d-17-0133.1.

Flores-Vidal, X., Durazo, R., Castro, R., Navarro, L.F., Dominguez, F., Gil, E., 2015. Fine-scale tidal and subtidal variability of an upwelling-influenced bay as measured by the mexican high frequency radar observing system. In: Coastal Ocean Observing Systems. Elsevier, pp. 209–228. http://dx.doi.org/10.1016/b978-0-12-802022-7.00012-2.

Gerbi, G.P., Trowbridge, J.H., Terray, E.A., Plueddemann, A.J., Kukulka, T., 2009. Observations of turbulence in the ocean surface boundary layer: Energetics and transport. J. Phys. Oceanogr. 39 (5), 1077–1096. http://dx.doi.org/10.1175/2008jpo4044.1.

Gross, T.F., Nowell, A.R.M., 1985. Spectral scaling in a tidal boundary layer. J. Phys. Oceanogr. 15 (5), 496–508. http://dx.doi.org/10.1175/1520-0485(1985)015<0496:ssiatb>2.0.co;2.

Guerra, M., Thomson, J., 2017. Turbulence measurements from five-beam acoustic Doppler current profilers. J. Atmos. Ocean. Technol. 34 (6), 1267–1284. http://dx.doi.org/10.1175/jtech-d-16-0148.1.

Hasselmann, K., Olbers, D., 1973. Measurements of wind-wave growth and swell decay during the joint north sea wave project (JONSWAP). Ergänzung Zur Deut. Hydrogr. Z., Reihe A 12 (8), 1–95.

Howarth, M., Souza, A., 2005. Reynolds stress observations in continental shelf seas. Deep. Sea Res. Part II: Top. Stud. Ocean. 52 (9–10), 1075–1086. http://dx.doi.org/10.1016/j.dsr2.2005.01.003.

Jones, N.L., Monismith, S.G., 2008. The influence of whitecapping waves on the vertical structure of turbulence in a shallow estuarine embayment. J. Phys. Oceanogr. 38 (7), 1563–1580. http://dx.doi.org/10.1175/2007jpo3766.1.

Kirincich, A.R., Lentz, S.J., Gerbi, G.P., 2010. Calculating Reynolds stresses from ADCP measurements in the presence of surface gravity waves using the cospectra-fit method. J. Atmos. Ocean. Technol. 27 (5), 889–907. http://dx.doi.org/10.1175/2009jtecho682.1.

Kirincich, A.R., Rosman, J.H., 2011. A comparison of methods for estimating Reynolds stress from ADCP measurements in wavy environments. J. Atmos. Ocean. Technol. 28 (11), 1539–1553. http://dx.doi.org/10.1175/jtech-d-11-00001.1.

Kolmogorov, A., 1991. Dissipation of energy in the locally isotropic turbulence. Proc.: Math. Phys. Sci. 434 (1890), 15–17, URL: http://www.jstor.org/stable/51981.

Lee, S.-H., Chang, Y.-S., 2019. Classification of the global tidal types based on auto-correlation analysis. Ocean. Sci. J. 54 (2), 279–286. http://dx.doi.org/10.1007/s12601-019-0009-7.

Lorke, A., Wüest, A., 2005. Application of coherent ADCP for turbulence measurements in the bottom boundary layer. J. Atmos. Ocean. Technol. 22 (11), 1821–1828. http://dx.doi.org/10.1175/jtech1813.1.

Lu, Y., Lueck, R.G., 1999a. Using a broadband ADCP in a tidal channel. Part I: Mean flow and shear. J. Atmos. Ocean. Technol. 16 (11), 1556–1567. http://dx.doi.org/10.1175/1520-0426(1999)016<1556:uabaia>2.0.co;2.

Lu, Y., Lueck, R.G., 1999b. Using a broadband ADCP in a tidal channel. Part II: Turbulence. J. Atmos. Ocean. Technol. 16 (11), 1568–1579. http://dx.doi.org/10.1175/1520-0426(1999)016<1568:uabaia>2.0.co;2.

Lumley, J.L., Terray, E.A., 1983. Kinematics of turbulence convected by a random wave field. J. Phys. Oceanogr. 13 (11), 2000–2007. http://dx.doi.org/10.1175/1520-0485(1983)013<2000:kotcba>2.0.co;2.

Mariotti, G., Fagherazzi, S., 2011. Asymmetric fluxes of water and sediments in a mesotidal mudflat channel. Cont. Shelf Res. 31 (1), 23–36. http://dx.doi.org/10.1016/j.csr.2010.10.014.

Martini, M., 2020. ADCPy. URL: https://github.com/mmartini-usgs/ADCPy.

Mateos, E., Marinone, S., Parés-Sierra, A., 2009. Towards the numerical simulation of the summer circulation in Todos Santos Bay, Ensenada, B.C. Mexico. Ocean. Model. 27 (1–2), 107–112. http://dx.doi.org/10.1016/j.ocemod.2008.11.002.

McMillan, J.M., Hay, A.E., 2017. Spectral and structure function estimates of turbulence dissipation rates in a high-flow tidal channel using broadband ADCPs. J. Atmos. Ocean. Technol. 34 (1), 5–20. http://dx.doi.org/10.1175/jtech-d-16-0131.1.

McMillan, J.M., Hay, A.E., Lueck, R.G., Wolk, F., 2016. Rates of dissipation of turbulent kinetic energy in a high Reynolds number tidal channel. J. Atmos. Ocean. Technol. 33 (4), 817–837. http://dx.doi.org/10.1175/jtech-d-15-0167.1.

Milne, I.A., Sharma, R.N., Flay, R.G.J., Bickerton, S., 2013. Characteristics of the turbulence in the flow at a tidal stream power site. Philos. Trans. R. Soc. A: Math. Phys. Eng. Sci. 371 (1985), 20120196. http://dx.doi.org/10.1098/rsta.2012.0196.

Nowacki, D.J., Ogston, A.S., 2013. Water and sediment transport of channel-flat systems in a mesotidal mudflat: Willapa Bay, Washington. Cont. Shelf Res. 60, S111–S124. http://dx.doi.org/10.1016/j.csr.2012.07.019.

Nystrom, E.A., Rehmann, C.R., Oberg, K.A., 2007. Evaluation of mean velocity and turbulence measurements with ADCPs. J. Hydraul. Eng. 133 (12), 1310–1318. http://dx.doi.org/10.1061/(asce)0733-9429(2007)133:12(1310).

Orton, P.M., Zappa, C.J., McGillis, W.R., 2010. Tidal and atmospheric influences on near-surface turbulence in an estuary. J. Geophys. Res.: Ocean. 115 (C12), http://dx.doi.org/10.1029/2010jc006312.

Osalusi, E., Side, J., Harris, R., 2009a. Reynolds stress and turbulence estimates in bottom boundary layer of Fall of Warness. Int. Commun. Heat Mass Transfer 36 (5), 412–421. http://dx.doi.org/10.1016/j.icheatmasstransfer.2009.02.004.

Osalusi, E., Side, J., Harris, R., 2009b. Structure of turbulent flow in EMEC's tidal energy test site. Int. Commun. Heat Mass Transfer 36 (5), 422–431. http://dx.doi.org/10.1016/j.icheatmasstransfer.2009.02.010.

Pawlowicz, R., Beardsley, B., Lentz, S., 2002. Classical tidal harmonic analysis including error estimates in MATLAB using T_TIDE. Comput. Geosci. 28 (8), 929–937. http://dx.doi.org/10.1016/s0098-3004(02)00013-4.

Pérez-Higuera, R., Chee-Barragán, A., 1984. Sediment transport in Todos Santos Bay, B.C.. Cienc. Mar. 10 (3), 31–52. http://dx.doi.org/10.7773/cm.v10i3.448.

Pope, S.B., Pope, S.B., 2000. Turbulent Flows. Cambridge University Press.

Reeve, D., Chadwick, A., Fleming, C., 2018. Coastal Engineering: Processes, Theory and Design Practice. Crc Press.

Rippeth, T.P., Simpson, J.H., Williams, E., Inall, M.E., 2003. Measurement of the rates of production and dissipation of turbulent kinetic energy in an energetic tidal flow: Red Wharf Bay revisited. J. Phys. Oceanogr. 33 (9), 1889–1901. http://dx.doi.org/10.1175/1520-0485(2003)033<1889:motrop>2.0.co;2.

Rippeth, T.P., Williams, E., Simpson, J.H., 2002. Reynolds stress and turbulent energy production in a tidal channel. J. Phys. Oceanogr. 32 (4), 1242–1251. http://dx.doi.org/10.1175/1520-0485(2002)032<1242:rsatep>2.0.co;2.

Rosman, J.H., Hench, J.L., Koseff, J.R., Monismith, S.G., 2008. Extracting Reynolds stresses from acoustic Doppler current profiler measurements in wave-dominated environments. J. Atmos. Ocean. Technol. 25 (2), 286–306. http://dx.doi.org/10.1175/2007jtecho525.1.

Ruiz de Alegria-Arzaburu, A., Vidal, J., 2017. Post-storm beach recovery capabilities after El Niño winter at Ensenada Beach, Mexico.

Sentchev, A., Thiébaut, M., Schmitt, F.G., 2020. Impact of turbulence on power production by a free-stream tidal turbine in real sea conditions. Renew. Energy 147, 1932–1940. http://dx.doi.org/10.1016/j.renene.2019.09.136.

Serio, F.D., Mossa, M., 2015. Analysis of mean velocity and turbulence measurements with ADCPs. Adv. Water Resour. 81, 172–185. http://dx.doi.org/10.1016/j.advwatres.2014.11.006.

Shcherbina, A.Y., D'Asaro, E.A., 2024. Wave-induced biases in ADCP measurements from quasi-Lagrangian platforms. http://dx.doi.org/10.48550/ARXIV.2405.00763, URL: https://arxiv.org/abs/2405.00763.

Simpson, J., Williams, E., Brasseur, L., Brubaker, J., 2005. The impact of tidal straining on the cycle of turbulence in a partially stratified estuary. Cont. Shelf Res. 25 (1), 51–64. http://dx.doi.org/10.1016/j.csr.2004.08.003.

Soloviev, A., Lukas, R., 2003. Observation of wave-enhanced turbulence in the near-surface layer of the ocean during TOGA COARE. Deep. Sea Res. Part I: Ocean. Res. Pap. 50 (3), 371–395. http://dx.doi.org/10.1016/s0967-0637(03)00004-9.

Souza, A.J., Howarth, M.J., 2005. Estimates of Reynolds stress in a highly energetic shelf sea. Ocean. Dyn. 55 (5–6), 490–498. http://dx.doi.org/10.1007/s10236-005-0012-7.

Stacey, M.T., Monismith, S.G., Burau, J.R., 1999. Measurements of Reynolds stress profiles in unstratified tidal flow. J. Geophys. Res.: Ocean. 104 (C5), 10933–10949. http://dx.doi.org/10.1029/1998jc900095.

Stapleton, K.R., Huntley, D.A., 1995. Seabed stress determinations using the inertial dissipation method and the turbulent kinetic energy method. Earth Surf. Process. Landf. 20 (9), 807–815. http://dx.doi.org/10.1002/esp.3290200906.

Sun, J., Liu, L., Lin, J., Lin, B., Zhao, H., 2020. Vertical water renewal in a large estuary and implications for water quality. Sci. Total Environ. 710, 135593. http://dx.doi.org/10.1016/j.scitotenv.2019.135593.

Terray, E., Donelan, M., Agrawal, Y., Drennan, W., Kahma, K., Williams, A., Hwang, P., Kitaigorodskii, S., 1996. Estimates of kinetic energy dissipation under breaking waves. J. Phys. Oceanogr. 26 (5), 792–807. http://dx.doi.org/10.1175/1520-0485(1996)026<0792:eokedu>2.0.co;2.

Terray, E.A., Drennan, W.M., Donelan, M.A., 1999. The vertical structure of shear and dissipation in the ocean surface layer. URL: https://api.semanticscholar.org/CorpusID:31891934.

Thiébaut, M., Filipot, J.-F., Maisondieu, C., Damblans, G., Duarte, R., Droniou, E., Chaplain, N., Guillou, S., 2020a. A comprehensive assessment of turbulence at a tidal-stream energy site influenced by wind-generated ocean waves. Energy 191, 116550. http://dx.doi.org/10.1016/j.energy.2019.116550.

Thiébaut, M., Filipot, J.-F., Maisondieu, C., Damblans, G., Duarte, R., Droniou, E., Guillou, S., 2020b. Assessing the turbulent kinetic energy budget in an energetic tidal flow from measurements of coupled ADCPs. Philos. Trans. R. Soc. A: Math. Phys. Eng. Sci. 378 (2178), 20190496. http://dx.doi.org/10.1098/rsta.2019.0496.

Thiébaut, M., Filipot, J.-F., Maisondieu, C., Damblans, G., Jochum, C., Kilcher, L., guillou, s.s., 2020c. Characterization of the vertical evolution of the three-dimensional turbulence for fatigue design of tidal turbines. Philos. Trans. R. Soc. A: Math. Phys. Eng. Sci. 378 (2178), 20190495. http://dx.doi.org/10.1098/rsta.2019.0495, URL: https://hal-ensta-bretagne.archives-ouvertes.fr/hal-02924135.

Trowbridge, J., Elgar, S., 2001. Turbulence measurements in the surf zone*. J. Phys. Oceanogr. 31 (8), 2403–2417. http://dx.doi.org/10.1175/1520-0485(2001)031<2403:tmitsz>2.0.co;2.

Vallis, G.K., 2017. Atmospheric and Oceanic Fluid Dynamics: Fundamentals and Large-Scale Circulation. Cambridge University Press, http://dx.doi.org/10.1017/9781107588417.

Wiles, P.J., Rippeth, T.P., Simpson, J.H., Hendricks, P.J., 2006. A novel technique for measuring the rate of turbulent dissipation in the marine environment. Geophys. Res. Lett. 33 (21), http://dx.doi.org/10.1029/2006gl027050.

Williams, E., Simpson, J.H., 2004. Uncertainties in estimates of Reynolds stress and TKE production rate using the ADCP variance method. J. Atmos. Ocean. Technol. 21 (2), 347–357. http://dx.doi.org/10.1175/1520-0426(2004)021<0347:uieors>2.0.co;2.

Zedel, L., 2001. Using ADCP background sound levels to estimate wind speed. J. Atmos. Ocean. Technol. 18 (11), 1867–1881. http://dx.doi.org/10.1175/1520-0426(2001)018<1867:uabslt>2.0.co;2.